Monthly Notices
of the
ROYAL ASTRONOMICAL SOCIETY

MNRAS **512,** 1541–1556 (2022)
Advance Access publication 2022 March 9

https://doi.org/10.1093/mnras/stac625

Metallicity estimation of core-collapse Supernova H II regions in galaxies within 30 Mpc

R. Ganss,[1] J. L. Pledger ,[1]★ A. E. Sansom ,[1] P. A. James,[2] J. Puls[3] and S. M. Habergham-Mawson[2]

[1]*Jeremiah Horrocks Institute, University of Central Lancashire, Preston PR1 2HE, UK*
[2]*Astrophysics Research Institute, Liverpool John Moores University, 146 Brownlow Hill, Liverpool L3 5RF, UK*
[3]*LMU München, Universitäts-Sternwarte, Scheinerstr. 1, D-81679 München, Germany*

Accepted 2022 March 3. Received 2022 March 1; in original form 2022 January 14

ABSTRACT

This work presents measurements of the local H II environment metallicities of core-collapse supernovae (SNe) within a luminosity distance of 30 Mpc. 76 targets were observed at the Isaac Newton Telescope and environment metallicities could be measured for 65 targets using the N2 and O3N2 strong emission line method. The cumulative distribution functions (CDFs) of the environment metallicities of Type Ib and Ic SNe tend to higher metallicity than Type IIP, however Type Ic are also present at lower metallicities whereas Type Ib are not. The Type Ib frequency distribution is narrower (standard deviation ∼0.06 dex) than the Ic and IIP distributions (∼0.15 dex) giving some evidence for a significant fraction of single massive progenitor stars; the low metallicity of Type Ic suggests a significant fraction of compact binary progenitors. However, both the Kolmogorov–Smirnov test and the Anderson–Darling test indicate no statistical significance for a difference in the local metallicities of the three SN types. Monte Carlo simulations reveal a strong sensitivity of these tests to the uncertainties of the derived metallicities. Given the uncertainties of the strong emission methods, the applicability of the tests seems limited. We extended our analysis with the data of the Type Ib/Ic/IIP SN sample from Galbany et al. The CDFs created with their sample confirm our CDFs very well. The statistical tests, combining our sample and the Galbany et al. sample, indicate a significant difference between Type Ib and Type IIP with <5 per cent probability that they are drawn from the same parent population.

Key words: supernovae: general – H II regions – galaxies: abundances.

1 INTRODUCTION

Massive stars are the key players in the chemical enrichment of the Universe. Their strong stellar winds and their ultimate death as core-collapse supernovae (SNe) enrich the interstellar medium with chemical elements burned during a star's lifetime and with new elements created in the SN explosion. To understand the details of the SN explosion process and the synthesis of heavy elements beyond iron, knowledge of the nature of SN progenitor stars is essential. It is commonly accepted that massive stars with masses >8 $M_{\odot}$ end their life in a core-collapse SN explosion (e.g. reviews by Crowther 2007; Smartt 2009), however the detailed links between the progenitor star parameters and the observed diversity of SN explosions are still uncertain.

Historically, the classification of SNe is mainly based on spectral features (e.g. Filippenko 1997; Turatto 2003) and divided into the two main types of hydrogen-poor Type I SNe and hydrogen-rich Type II SNe, in which all but sub-type Ia (thermonuclear explosion, see e.g. Maoz, Mannucci & Nelemans 2014 for a review) are core-collapse SNe.

The hydrogen-poor Type I core-collapse SNe are further divided into sub-types Ib and Ic by features in the early spectrum around peak luminosity: Type Ib spectra show strong helium but no hydrogen absorption lines, Type Ic spectra have neither hydrogen nor helium lines.

The hydrogen-rich Type II SNe are divided into four sub-types IIL, IIP, IIn, and IIb. Spectra of the most abundant types IIP and IIL are characterized by broad hydrogen emission lines (e.g. Gutiérrez et al. 2017) indicating high expansion velocities of the SN ejecta. They are differentiated by the shape of their light curves: Light curves of Type IIP have a distinct plateau phase after the peak luminosity with almost constant or slowly declining luminosity, in contrast to the light curve of Type IIL showing a steady (more or less linear) decrease after the peak luminosity. Recent evidence does not support this strict separation between Type IIP and Type IIL but a continuous range of decay rates of Type II SNe (Anderson et al. 2014; Sanders et al. 2015; Galbany et al. 2016a; Valenti et al. 2016). Type IIn SNe, first introduced by Schlegel (1990), are characterized by relatively narrow Balmer emission lines indicating strong interaction of SNe shock waves with dense circumstellar material (e.g. Taddia et al. 2013a). Type IIb SNe have an intermediate character between Type II and Type Ib SNe and exhibit hydrogen lines in the early, photospheric phase which disappear in the later nebular phase when the ejecta become optically thin (e.g. Fang & Maeda 2018).

In addition to the regular core-collapse SN types, there are high energetic SNe events ('Hypernovae') not fitting into the scheme above. They are generally classified as Type Ibc-pec, also named as Types Ic-bl (very broad lines in spectrum, e.g. Taddia et al. 2019) or Type Ic-GRB (associated by a gamma-ray burst; e.g. Woosley &

★ E-mail: jpledger@uclan.ac.uk

© 2022 The Author(s)
Published by Oxford University Press on behalf of Royal Astronomical Society

Downloaded from https://academic.oup.com/mnras/article/512/1/1541/6545806 by University of Central Lancashire user on 23 March 2022

Bloom 2006). A class of its own are superluminous SNe with absolute magnitudes $M_V < -21$ mag (e.g. Gal-Yam 2019; Chen 2021).

The diversity of SNe types reflects the diversity of unknown parameters of SNe progenitors, with initial mass, age, metallicity, and binarity as the most important parameters. Additionally, the nature of the progenitor has to explain the observed spectral lines of Type Ibc[1] SNe. An absence of hydrogen (and helium) lines suggest the loss of the outer envelopes of the progenitor star before the explosion, which is possible by two fundamentally different channels: either the progenitor is an evolved single massive ($M_{ZAMS} \geq 25 - 30\ M_\odot$) Wolf–Raye (WR) star (see Crowther 2007 for a review) losing its outer envelopes by strong stellar winds (e.g. Kudritzki & Puls 2000; Vink & de Koter 2005; Smith 2014), or it is a less massive star in a close binary system losing its outer envelopes to the companion by accretion (e.g. Podsiadlowski, Joss & Hsu 1992; Eldridge, Izzard & Tout 2008; Yoon, Woosley & Langer 2010; Dessart et al. 2011).

The most direct way to constrain the progenitor of a core-collapse SNe is to use archival images of the explosion site to identify the progenitor star. This approach has been successful for Type II SNe (e.g. Smartt 2015; Van Dyk 2017 and references therein). A statistically significant number of progenitor stars of the abundant Type IIP SNe have been identified as red supergiants (RSGs) with initial masses between $8\ M_\odot$ and $17\ M_\odot$ (Smartt 2009; Van Dyk 2017). Type IIL SNe are quite rare but the few direct progenitor detections indicate an initial progenitors mass $\leq 25\ M_\odot$ (e.g. 2009kr, Elias-Rosa et al. 2010; SN2009hd, Elias-Rosa et al. 2011; SN1996al, Benetti et al. 2016) and all appear to have a low-mass H-envelope. A few direct detections of Type IIn progenitors have been reported (e.g. SN2005gl, Gal-Yam & Leonard 2009; SN2009ip, Foley et al. 2011; SN2010jl, Smith et al. 2011b), pointing to luminous blue variable stars as progenitors, but these detections are still ambiguous. The same ambiguity applies to Type IIb progenitor detections (e.g. SN1993J, Aldering, Humphreys & Richmond 1994; Van Dyk et al. 2002; Maund et al. 2004; SN2008ax, Crockett et al. 2008; SN2011dh, Maund et al. 2011; Van Dyk et al. 2011; SN2013df, Van Dyk et al. 2014; SN2016gkg, Tartaglia et al. 2017), which suggest a variety of progenitors including RSGs or yellow supergiants, with or without a companion.

The direct detection of progenitors of Type Ibc SNe has been challenging and is complex. Binarity can play a crucial role in defining the SN subtype, however with pre-explosion imaging it is difficult to differentiate a low-mass binary system from a single high mass star. Consequently, the binary/single-star debate is unsolved for all direct detections of Type Ibc progenitors. One of the most studied and debated direct progenitor detections is the case of the Type Ib SN iPTF13bvn (Cao et al. 2013; Groh, Georgy & Ekstrom 2013; Bersten et al. 2014; Fremling et al. 2014; Eldridge et al. 2015; Kuncarayakti et al. 2015; Eldridge & Maund 2016; Folatelli et al. 2016; Hirai 2017) resulting in the still open question of whether the progenitor was a massive star or a close binary system. Most recently, Kilpatrick et al. (2021) reported a pre-explosion image detection of the progenitor of the Type Ib SN2019yvr, inferring a cool and inflated progenitor, but again were unable to rule out a close binary scenario. The only direct detection of a Type Ic SN progenitor is for SN2017ein (Kilpatrick et al. 2018; Van Dyk et al. 2018), however the results of these two studies are unable to distinguish between a high initial mass single star (M_{ZAMS} 47–55 $M_\odot$), a close binary with two high mass components ($80 + 48\ M_\odot$), or a young compact star cluster. The study by Xiang et al. (2019) additionally took advantage of very early (1–2 d after explosion) photometric and spectral data of SN2017ein and derived consistent constraints for the progenitor. In contradiction, Teffs et al. (2021) derived a lower mass progenitor (16–20 $M_\odot$) from modelling of photospheric and nebular phase spectral data. Further observations of the SN2017ein explosion site are required to solve this disagreement and further constrain the progenitor.

Many studies searching for Type Ibc progenitors failed with the direct detection but provided upper limits for the luminosity and mass of the progenitors (e.g. SN1994I, Barth et al. 1996; Van Dyk, de Mink & Zapartas 2016; SN2000ew, Maund & Smartt 2005; SN2001B, Maund & Smartt 2005; SN2002ap, Mazzali et al. 2002; Smartt et al. 2002; Crockett et al. 2007; SN2004gt, Maund, Smartt & Schweizer 2005; Gal-Yam et al. 2005; SN2009jf, Valenti et al. 2011; SN2012au, Pandey et al. 2021; SN2012fh, Johnson, Kochanek & Adams 2017; SN2013dk, Elias-Rosa et al. 2013). Because the majority of these studies found upper luminosity limits too low for single massive WR stars, the binary formation channel is currently favoured for the stripped-envelope Type Ibc SNe. This is supported by arguments related to the stellar initial mass function (IMF) and the observed ratio of Type Ibc to Type II SNe (e.g. Smartt 2009). However, the binary channel for Type Ibc SNe is not definitely established and the single massive WR star cannot be ruled out (e.g. Smith et al. 2011a).

Given the challenges of direct progenitor detection, other studies have investigated the variation of Type Ibc to Type II ratio with global properties of the host galaxies to constrain SN progenitors (e.g. Prantzos & Boissier 2003; Prieto, Stanek & Beacom 2008; Boissier & Prantzos 2009; Arcavi et al. 2010; Hakobyan et al. 2014, 2016). However, the multiple stellar populations of the hosts with their different ages, metallicities, and star formation histories make it difficult to produce useful constraints on progenitors. To avoid such complications, most studies have tried to constrain progenitor properties from the local SN environment using either global proxies to derive the local parameters or by direct observations of the local SN environment (see Anderson et al. 2015 for a review). The motivation behind this approach is that a massive progenitor star can only travel a short distance from the place of birth to the observed explosion site due to its short lifetime. Therefore, age and metallicity of the stellar population and H II region at the explosion site should be representative of the SN progenitor itself.

Early work on SN environments by Van Dyk & Schuyler (1992) found that approximately 50 per cent of SNe were associated with a H II region with no significant difference between Type II and Type I SNe. In contrast, Anderson & James (2008) found only a small fraction of Type II SNe associated with H II regions, whereas an association for Type Ibc was found. They used the pixel statistics technique (Fruchter et al. 2006; James & Anderson 2006) with narrow-band Hα images and concluded that Type Ibc progenitors are more massive than Type II (Anderson & James 2008). Crowther (2013) argued that there should be no association between Type II SNe and H II regions because the lifetime of typical H II regions are considerably shorter than the lifetime of RSGs. Maund (2018) evaluated the very young resolved stellar populations in the environments of stripped-envelope SNe and found decreasing characteristic ages of the populations from Type IIb, Type Ib to Type Ic (log(age) = 7.20, 7.05, and 6.57, respectively). The finding indicates a significant fraction of massive stars as progenitors of Type Ibc SNe.

The metallicity of an SN progenitor is of particular interest because it determines – together with the luminosity – the strength of the stellar winds and consequently the mass-loss of the progenitor (predicted mass-loss rate $\dot{M} \propto Z^{0.42-0.85}$; Vink & Sander 2021). Studies based on global proxies have used the radial position of

[1]throughout this paper 'Type Ibc' means 'Type Ib and Ic', while 'Ib/c' means a Type I core-collapse SN with ambiguous classification.

Downloaded from https://academic.oup.com/mnras/article/512/1/1541/6545806 by University of Central Lancashire user on 23 March 2022

the explosion sites together with the host central metallicities and the metallicity gradient of galaxies (e.g. Henry & Worthey 1999 for a review) to constrain the progenitor metallicity (e.g. Prieto et al. 2008; Anderson & James 2009; Taddia et al. 2016). However, studies with indirect measurement of metallicity at explosion sites derived from global proxies suffer from large uncertainties caused by e.g. galaxy interactions, recent galaxy mergers, or unknown star formation history. Consequently, the direct measurement of gas metallicity at the local environments of SNe explosion sites is preferred.

Several studies (Modjaz et al. 2008; Anderson et al. 2010; Leloudas et al. 2011; Modjaz et al. 2011; Kelly & Kirshner 2012; Sanders et al. 2012; Kuncarayakti et al. 2013a, b, 2018; Taddia et al. 2013b, 2015; Galbany et al. 2016b, c, 2018; Krühler et al. 2017; Schady et al. 2019; Xiao et al. 2019) have measured the gas-phase metallicities of the H II regions at the SN explosion sites based on long-slit or integral field spectroscopy applying empirical strong emission line methods. Results of these studies are inconclusive and do not unambiguously constrain progenitor metallicities for different types of SNe. The majority of studies concluded that environments of Type Ibc SNe tend to have higher metallicities than environments of Type II SNe, but the differences were not statistically significant.

Despite all the effort to constrain the physical parameters of SNe progenitors, most questions remain unanswered. This work presents metallicity data of the environments of a well-defined, volume-limited, large sample of SNe within a distance of 30 Mpc based on long-slit spectroscopic data and inferred by the strong emission line method. The paper is structured as follows: Section 2 presents the SN sample selection criteria and the target observations. Section 3 describes the data reduction process and the method of SN environment metallicity measurement. Section 4 presents the results followed by the discussion in Section 5. Finally, Section 6 summarizes the conclusions.

2 OBSERVATIONS OF SN SITES

This project aims to evaluate differences in the metallicity of the environments of different core-collapse SN types based on a large sample of volume-limited SN detections. The sample was compiled according to selection criteria as follows: (i) Luminosity distance $\lesssim$ 30 Mpc in order to get an appropriate spatial resolution and to avoid greater uncertainties of true local metallicity at higher redshifts, (ii) reliable spectral SN classification as Type IIP, Type Ib, or Type Ic to avoid any skew by uncertain classifications, and (iii) the host galaxy should have sufficiently low inclination ($<75^\circ$) to avoid ambiguities of the SN H II region identification and to avoid issues with emission lines detection by high host extinction.

SNe with luminosity distances up to 33 Mpc were taken from the Open Supernova Catalogue[2] (Guillochon et al. 2017). All SNe up to 27 Mpc were accepted as target candidate. The luminosity distances of SNe between 27 and 33 Mpc were searched for additional distance measurements in the NASA/IPAC Extragalactic Database (NED;[3] Helou et al. 1991) and accepted as candidate if distances <30 Mpc are consistently reported.

Classifications of the SNe were taken from the Open Supernova Catalogue. All SNe with clear Type Ib, Type Ic, and Type IIP were accepted as targets. There is a large diversity in Type II subtypes (IIP. IIL, IIn, IIb) and Graham (2019) presents work suggesting that different Type II subtypes have different metallicity distributions, although low number statistics for the rarer subtypes makes this difficult to confirm. To ensure this diversity does not affect our results we include only Type IIP SNe, which are abundant in number and have many confirmed RSG progenitors (Smartt 2009).

SNe with ambiguous classification as 'Type Ib/c' or just 'Type II' were examined by the references given in the Open Supernova Catalogue and assigned the subtype most commonly reported in the literature. Additionally, SNe older than 1990 were excluded because of uncertainties of the instrumentation and of the classification method used. SNe younger than 2017 were excluded to avoid a potential contamination of the H II region by (residual) light of the SN event itself.

Inclinations of the host galaxies were taken from Hyperleda[4] (Makarov et al. 2014). The inclination of the host galaxy is the least constraining criterion. The light of an SN environment in the outskirts of a high inclination galaxy may be less affected by stellar contamination than the light of an SN environment close to the centre of a low inclination galaxy. Thus, all SNe in hosts with inclination $<75^\circ$ were accepted as candidate and SNe in hosts with an inclination $>75^\circ$ were decided case-by-case depending on the location of the SN in the galaxy. This approach identified 40 Type Ib, 39 Type Ic, and 107 Type IIP SNe as target candidates for the project.

Observational data were taken over five observational periods between 2016 September and 2019 February (Table 1) at the Isaac Newton Telescope (INT) on La Palma with the IDS/EEV10 instrument with the technical configuration shown in Table 2. A total of 96 observations, of 76 individual SNe (Table A1), were obtained over 19 nights. Eleven targets were observed twice and two targets were observed three times to get an improved signal-to-noise ratio (SNR) and to check our methods for consistency/reproducibility.

An additional four targets (SN1990aa, SN1991ar, SN1996D, and SN2009ga), which are not part of the selected target sample, could be observed by opportunity. The data of these four targets were reduced and evaluated but their data are not incorporated in the statistical evaluation in Section 4 because the luminosity distance is significantly larger than 30 Mpc (lower uncertainty range limit >40 Mpc).

The observations include the standard calibration frames (bias and flat frames, arc frames for wavelength calibration, standard star frames for flux calibration). In order to remove cosmic rays, it was aimed to take three exposures for every target observation, which worked for all but three targets. Exposure time was typically 1200s per frame increased for faint targets and/or high sky brightness conditions up to 1800s per frame. Seeing conditions were between 0.8 and 1.2 arcsec for all observation nights.

Table 1. Overview of the five INT observations runs contributing observation data to the project.

Year	Nights	#nights	#obs.	INT prop. ID
2016	27-Sep to 01-Oct	5	25	I/2016B/05
2017[1]	27-Dec, 28-Dec	2	14	I/2017B/01
2018	18-Feb, 13-Jun, 30-Oct, 26-Nov	4	8	SI2018a02
2019	21-Feb, 22-Feb	2	10	SI2018a02
2019	23-Feb to 28-Feb	6	39	I/2019A/01

Notes. [1] Eight nights were allocated but the run was hindered by technical fault with the telescope for the first six nights for which additional discretionary director time was awarded under proposal ID S12018a02.

[2] https://sne.space
[3] http://ned.ipac.caltech.edu
[4] http://leda.univ-lyon1.fr

Downloaded from https://academic.oup.com/mnras/article/512/1/1541/6545806 by University of Central Lancashire user on 23 March 2022

Table 2. Technical configuration of IDS/EEV10 equipment for taking the calibration and science frames.

Spectrograph	IDS
Slit width	1.5 arcsec
Slit length	3.3 arcmin
Grating	R400V
Central wavelength	5802.4 Å
Dispersion	1.41 Å px^{-1}
Resolving power ($\lambda/\Delta\lambda$)	1596@4500 Å
Resolution ($\Delta\lambda$)	2.87 Å
Filters	Clear
Detector	EEV10
Readout speed	Slow
Linearity	±0.2 per cent to 65535 ADU
Saturation level	65535 ADU
Dark current	4 e h^{-1} @ 153 K
Gain factor	1.2 electrons/ADU
Scale factor	0.4 arcsec px^{-1}

3 DATA REDUCTION

The data reduction made use of the two standard astronomical software packages IRAF (Image Reduction and Analysis Facility; Tody 1986) and STARLINK (Currie et al. 2014).

Standard data reduction processes were carried out to reduce and combine the 2D spectra. Due to a slight variation of the bias level during some nights, bias subtraction was done by means of the individual bias strip of the frames. Dark current correction was negligible because of the detector cooling. The data reduction included S-distortion correction and flux calibration was achieved using standard star observations taken throughout the night. The spectra were trimmed to 3500–7000 Å given the location of the diagnostic lines required.

The pixel position of the SN site was identified and extracted from the reduced 2D spectrum. Evaluation of the correct SN site requires evaluation of the slit-orientation, which may differ from the position angle (PA) on the sky by ±180°. This was done by means of the INT acquisition images. With knowledge of the slit-orientation, the pixel row of the SN site spectrum was identified by the known angular distance of the SN site (Table A1) from host galaxy centre and the INT IDS spatial plate scale of 0.4 arcsec px^{-1} (Table 2). Extraction of the SN site spectrum was done by the IRAF APALL task with an extraction aperture of 4 arcsec as a reasonable choice to account for seeing conditions, INT guiding accuracy, and other imperfections in the optical path. The chosen 4 arcsec extraction aperture corresponds to a linear size of 19.4 pc Mpc^{-1} or about 0.6 kpc for a host galaxy with luminosity distance 30 Mpc.

Interstellar extinction for each SN region was derived from the Balmer line emission based on a H α/H β ratio of 2.86, assuming case B recombination (Hummer & Storey 1987) and empirical extinction curves from Osterbrock & Ferland (2006). Line emission was measured using the Emission Line Fitting (ELF) routine in the STARLINK package DIPSO and extinction correction was performed using the DRED routine. Target spectra lacking H β emission were only corrected for Galactic extinction towards the SN host galaxy with values taken from NED (based on Schlafly & Finkbeiner 2011) and assuming a Fitzpatrick (1985) reddening law. Fig. 1 shows an example of the final extracted spectrum with the most prominent emission lines indicated.

For flux calculation, the emission lines were fitted by Gaussian profiles using the DIPSO command ELF. The ELF fits have been done in the H α and in the H β region independently, but the fits within each region, i.e. H α/[N II] lines and H β/[O III] lines, respectively, have been done simultaneously. From all observations, 10 targets were affected by strong stellar contamination clearly visible by underlying broad absorption features at the H β emission line. The ELFcommand is not able to disentangle the emission lines flux from this stellar absorption at the same wavelength. To account for this absorption the fitting has been modified as follows: (i) cut the emission line affected by stellar contamination from the spectrum; (ii) fit the absorption feature by ELF, and (iii) subtract the Gaussian fit of the absorption feature from the initial spectrum, leaving just the emission line (see example in Fig. 2 for target SN2004fc). This worked well for all affected targets with strong stellar contamination and as long as the underlying absorption line is broader than the emission line. If the stellar absorption has a width less than or equal to the emission line width, then the workaround is not applicable because the emission line masks the absorption (see discussion in Section 5.5). A stellar contamination of the H α lines was not visible at all and estimated as negligible compared to the strength of H α line (see also Section 5.5).

The project made use of the empirical strong emission line method for measuring the metallicity of SNe environments, because the auroral [O III] λ4363 line required for the direct method is weak and often undetected. The strong emission line method uses only the flux ratios of strong nebular emission lines, which are much easier to detect, for the metallicity determination. The methods provide the ratio of the number density oxygen to hydrogen (in terms of 12+log(O/H)) as a proxy for metallicity.

Many different ratios of strong emission lines have been used to determine gas-phase metallicities (see e.g. Kewley & Ellison 2008; Kewley, Nicholls & Sutherland 2019, and references therein). The empirical approach of the method requires a calibration with a large number of H II regions, for which both the inferred metallicities by strong emission lines and the metallicity derived by the direct method, are known. This work uses the N2 and O3N2 methods introduced by Pettini & Pagel (2004) with the updated calibration by Marino et al. (2013), where the N2 indicator is defined by

$$\mathrm{N2} = \log\left(\frac{[\mathrm{N\ II}]\lambda6583}{\mathrm{H}\,\alpha}\right) \tag{1}$$

and the O3N2 indicator is defined by

$$\mathrm{O3N2} = \log\left(\frac{[\mathrm{O\ III}]\lambda5007/\mathrm{H}\,\beta}{[\mathrm{N\ II}]\lambda6583/\mathrm{H}\,\alpha}\right). \tag{2}$$

The N2 and O3N2 methods have been chosen because they use closely spaced emission line ratios making the methods robust to reddening and flux calibration issues. Additionally, these two methods are consistent with spectroscopically derived massive star abundances (Davies et al. 2017).

4 RESULTS

The H α and [N II] λ6583 emission lines required for the N2 indicator were detected in 66 of the 76 observed SNe environments. The O3N2 method additionally needs H β and [O III] λ5007 lines, which were detected in 46 observations. Metallicity estimation was not possible for 10 observed targets because either no emission lines were detected (SN1995bb, SN2003ie, SN2004ez, SN2005cz, SN2007od) or only hydrogen lines were present (SN1999ev, SN2005ad, SN2010br, SN2015aq, SN2017iro). We note that these SNe are a mix of SN subtypes.

Table A2 shows the measured metallicities of the SN environments inferred by N2 and O3N2 (where applicable) methods. M13-N2 and

Downloaded from https://academic.oup.com/mnras/article/512/1/1541/6545806 by University of Central Lancashire user on 23 March 2022

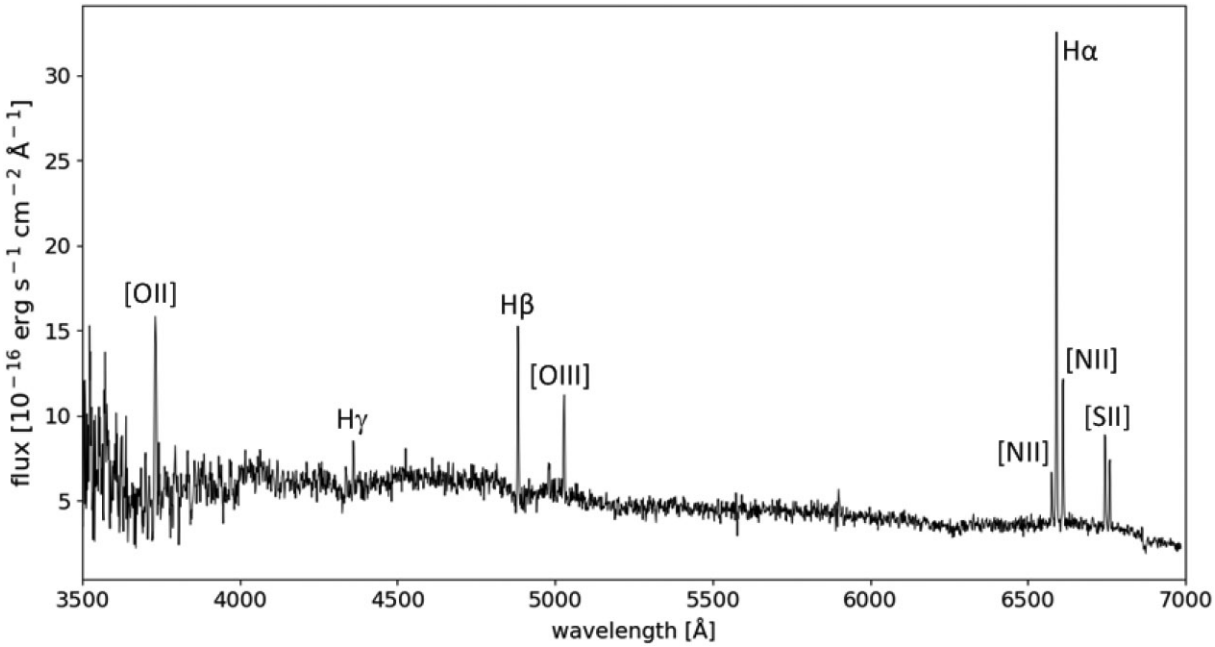

Figure 1. Obtained INT spectrum of Type Ib SN2012au environment as an example for the extracted 1D environment spectra. The figure shows the most prominent emission lines of which H α, [N II] λ6583, H β, and [O III] λ5007 have been used for the metallicity estimation.

M13-O3N2 are the results for the calibration by Marino et al. (2013) accordingly calculated by the equations

$$\text{M13-N2} = 8.743 + 0.462 \times \text{N2} \quad (3)$$

and

$$\text{M13-O3N2} = 8.533 - 0.214 \times \text{O3N2} \quad (4)$$

For compatibility with previous studies, the columns PP04-N2 and PP04-O3N2 present the results with the initial calibration by Pettini & Pagel (2004), calculated by

$$\text{PP04-N2} = 8.90 + 0.57 \times \text{N2} \quad (5)$$

and

$$\text{PP04-O3N2} = 8.73 - 0.32 \times \text{O3N2} \quad (6)$$

The statistical uncertainties resulting from the calibration itself are $\pm$0.16 dex for M13-N2, $\pm$0.18 dex for M13 O3N2 (1σ values, Marino et al. 2013), $\pm$0.18 dex for PP04-N2 and $\pm$0.14 dex for PP04-O3N2 (1σ values, Pettini & Pagel 2004). The observational uncertainties of our observed data by the photon noise and the data reduction process have been estimated to between $\pm$0.01 and $\pm$0.04 dex mainly depending on the SNR. This uncertainty is significantly less than the calibration uncertainties, and so has been neglected for simplicity.

For completeness, Table A3 shows the metallicities of the environments of SN1990aa, SN1991ar, SN1996D, and SN2009ga observed by opportunity. These four 'opportunity' targets do not show any remarkable difference to the metallicities of Table A2.

The N2 metallicities for 14 Type Ib, 19 Type Ic, and 33 Type IIP SN environments are obtained and O3N2 metallicities have been derived for 9 Type Ib, 18 Type Ic, and 19 Type IIP SN environments, and are presented in Table A2. SN2000ds, a Ib SN, has been excluded from the statistical evaluation as it has been classified as a Ca-rich SN (e.g. Filippenko et al. 2003). Such events are predicted to be part of the Ca-rich gap transients which are a different class of transients often found on the outskirts of elliptical galaxies suggesting an old (and hence low mass) progenitor population (Lyman et al. 2013; Lunnan et al. 2017; Shen, Quataert & Pakmor 2019). This leaves 13 Type Ib SN available for statistical evaluation with the N2 indicator; we note that no O3N2 result is available for SN2000ds.

Table 3 lists the mean and standard deviation of metallicities for different SN types and for the total sample. Differences in the mean metallicities for each subtype are small, with the largest difference being between Ib and IIP SN at 0.08 dex for the O3N2 calibration, but this is not statistically different if the standard error on the mean is considered and is not seen in the N2 calibration results. However, both calibrations indicate a large difference between the standard deviation of Type Ib SN compared to the two other subtypes. There is a factor of 2.0 (2.5) between Type Ib and both Type IIP/Ic standard deviations for the N2 (O3N2) calibrations, which is remarkable. The implications of this result are discussed in Section 5.5.

Fig. 3 shows the normalized cumulative distribution functions (CDFs) of the results for M13-N2 and M13-O3N2 calibrations. Reflecting the results presented in Table 3, there seem to be two clear tendencies in the CDF estimated by M13-O3N2 calibration: first, the mean metallicity of Type Ibc environments show a tendency to be higher (0.08 dex) than that of Type IIP and, secondly, the distribution of Type Ib is significantly narrower than the distribution of the two other types, indicating a restricted metallicity range for Ib SNe. (Type Ib standard deviation 0.06 dex compared to 0.16 dex; see Table 3). The first tendency above is not visible in the M13-N2 calibrations but the narrower distribution of Type Ib is still present.

In order to evaluate for statistically significant differences between the samples of the different SN-types, two statistical tests have been applied: the two-sample Kolmogorov–Smirnov test (KS-test) and the two-sample Anderson–Darling test (AD-test). Both tests are applicable for small samples (see e.g. tables in Massey 1952 and Pettitt 1976).

The tests have different approaches (schematically shown in Fig. 4) to test the null hypothesis that two discrete samples are drawn from

Downloaded from https://academic.oup.com/mnras/article/512/1/1541/6545806 by University of Central Lancashire user on 23 March 2022

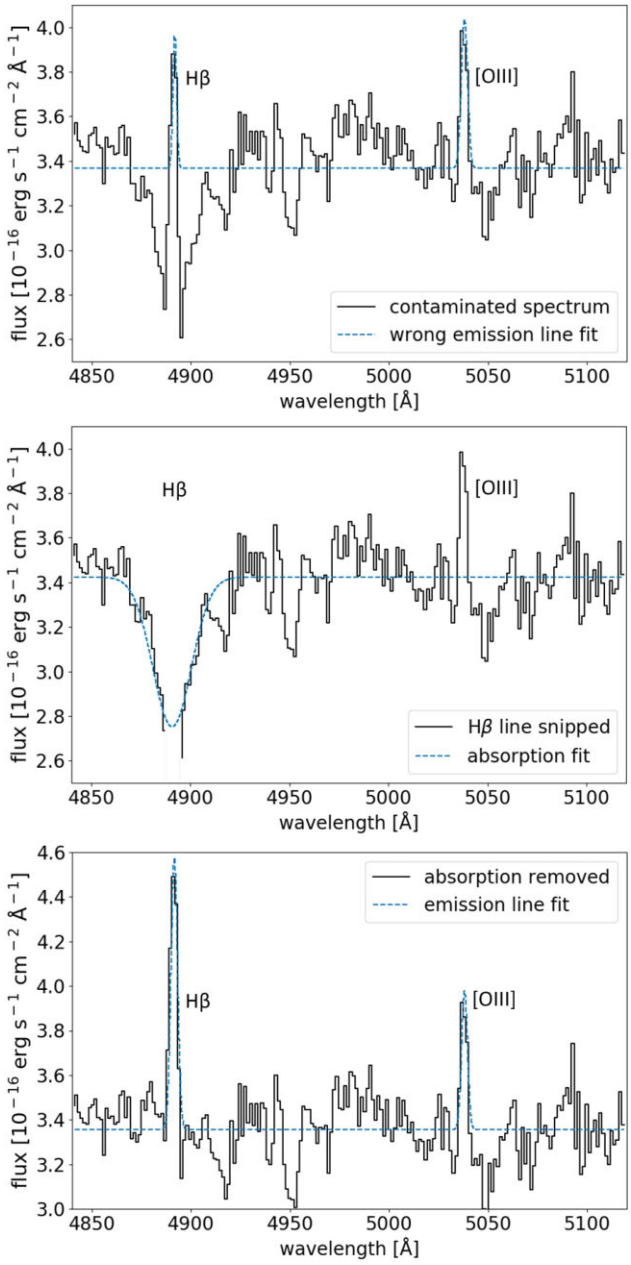

Figure 2. Underlying stellar contamination may affect the H β emission lines. This figure demonstrates the DIPSO workaround for the example SN2004fc as described in the text. The top plot shows the observed spectrum (black) of SN2004fc; the blue dashed line is the DIPSO ELF fit strongly affected by the contamination. The middle plot is the DIPSO fit to the absorption after snipping the H β line out of the observed spectrum. The bottom plot shows the improved emission line fit after removal of the stellar contamination by applying the absorption fit from the middle plot.

same parent population. The two-sample KS-test (e.g. Press 1988) calculates differences between two discrete samples by evaluation of the supremum $D = \sup_x|F_n(x)- G_m(x)|$ of the distances between two CDFs $F_n(x)$ and $G_m(x)$ (Fig. 4, left-hand panel) of two samples with sizes n and m, respectively. If the value of the supremum exceeds a critical value D_{crit}, the null hypothesis will be rejected and the two samples do not have the same parent population at certain significance. The value of D_{crit} is calculated by the Kolmogorov distribution (Marsaglia, Tsang & Wang 2003) and depends on the significance level α (usually 5 per cent or 1 per cent) and the sizes n and m of the two samples.

While the KS-test evaluates just the supremum of the distances between the CDFs of two samples, the AD-test takes into account all distances between the two CDFs (Fig. 4, right-hand panel). Consequently, differences in the tails of the CDFs are more weighted and the AD-test judges more the area between the CDFs than just a maximum value. Mathematically, the two-sample AD-test calculates a value A^2_{nm} by:

$$A^2_{nm} = \frac{nm}{N}\int_{-\infty}^{\infty}\frac{[F_n(x) - G_m(x)]^2}{H_N(x)\,[1 - H_N(x)]}\,dH_N(x) \quad (7)$$

(Pettitt 1976), where $F_n(x)$ and $G_m(x)$ are the CDFs of the two samples with sizes n and m, $N = n + m$ and $H_N(x)$ is the CDF of the combined sample of the two samples given by: $H_N(x) = [nF_n(x) + mG_m(x)]/N$ (Pettitt 1976).

The two-sample KS-test and AD-test are implemented in this work using the package 'twosamples' of the statistical software called 'R'[5] (Dowd 2020). The statistical tests of the package 'twosamples' are not based on tables to calculate the *p*-value of the given samples but perform real permutations between samples to evaluate the *p*-value. The null hypothesis, that both samples have same parent population, must be rejected if the *p*-value is less than the chosen significance level α.

Table 4 lists the *p*-value results of the sample combinations Ib-Ic, Ib-IIP, and Ic-IIP for M13-N2 and M13-O3N2 metallicity calibrations for both the two-sample KS-test and the two-sample AD-test. The *p*-value for a significance level of 5 per cent must be <0.05 to reject the null hypothesis. The *p*-values in Table 4 are all significantly greater than 0.05 and thus the null hypothesis is not rejected. The KS-test and AD-test detect no statistically significant difference of the SN environment metallicity between the different SN subtypes. Table 4 also shows the *p*-values of the test of Type Ib with the combined sample Ic + IIP. If the parent populations of Type Ic and Type IIP are the same, then the *p*-value of the combined sample test should be lower than the *p*-values of the single samples Ic and IIP, respectively. This is not the case; the test provides no statistical evidence that Type Ic and Type IIP have same parent population in agreement with observational findings.

5 DISCUSSION

The reliability of the results presented in Section 4 has been investigated by several measures: impact of stellar contamination, reproducibility of the results, reliability of the N2 and O3N2 calibrations, and effect of the metallicity uncertainties on the final *p*-value have been investigated using Monte Carlo (MC) simulations of the KS- and AD-test.

5.1 Stellar contamination

As discussed in Section 3 a H II region spectrum may be contaminated by stellar radiation of stars within the H II region and/or stars along the line of sight. This stellar contamination especially affects the hydrogen lines resulting in an underlying absorption impacting the true emission line flux.

The DIPSO workaround applied to remove stellar contamination does not work if the stellar absorption has a width less than or equal to the emission line width. For this reason the metallicity results of

[5] https://www.r-project.org

Downloaded from https://academic.oup.com/mnras/article/512/1/1541/6545806 by University of Central Lancashire user on 23 March 2022

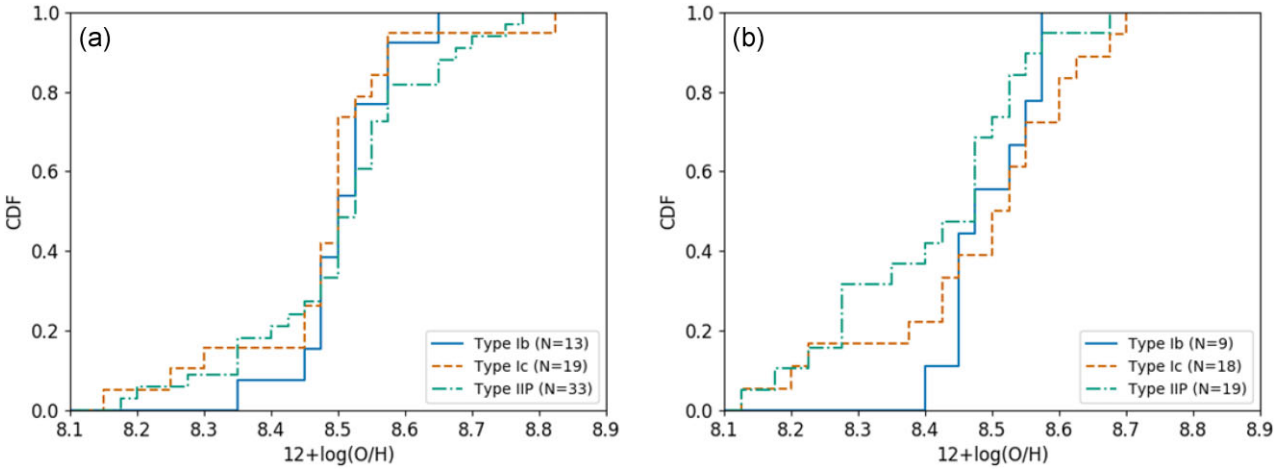

Figure 3. CDFs of the SN environment metallicities measured with the M13-N2 (left-hand panel) and M13-O3N2 (right-hand panel) calibration. Binning width for CDF calculation: 0.025 dex.

Table 3. Number of targets (N), mean values, and standard deviations (σ) of the metallicities split into the three SN types and for the total sample based on the M13-N2 and M13-O3N2 calibration results.

SN type	N(N2)	M13-N2 [12 + log(O/H)] mean	σ	N(O3N2)	M13-O3N2 [12 + log(O/H)] mean	σ
Ib	13	8.52	0.07	9	8.50	0.06
Ic	19	8.49	0.14	18	8.49	0.16
IIP	33	8.52	0.14	19	8.42	0.15
all	65	8.51	0.13	46	8.46	0.14

Table A2 have been checked independently by the more sophisticated penalized PiXel Fitting (pPXF) method of emission line fitting (Cappellari & Emsellem 2004; Cappellari 2017). Using synthetic spectral templates of stars with varying parameters (available e.g. from the MILES stellar population library,[6] Vazdekis et al. 2010) the observed continuum spectrum is fit allowing stellar kinematics and population parameters as well as the emission line flux to be extracted. The tests with pPXF reveal stellar contamination for most targets with H β emission lines flux generally more strongly affected than H α emission (as expected for a contamination by a young massive star population). However, the derived metallicities based on the fluxes from pPXF line fitting and DIPSO line fitting are consistent within $\pm$0.03 dex in the majority of targets. For 7 out of 65 M13-N2 measurements the metallicities differ significantly (>0.1 dex), however this is mainly because of numerical issues of pPXF and/or DIPSO caused by low SNR observations. The differences between the pPXF and DIPSO metallicities of these seven measurements are well within the uncertainty given by the calibration and do not affect the global M13-N2 results.

5.2 Reproducibility

There are 11 targets observed twice and two targets observed three times during the project allowing us to evaluate the reproducibility of results. Fig. 5 compares the metallicity for the multiple observed targets. The differences are all but one within the observational uncertainty of ~0.04 dex caused by the photon noise and the data reduction process. The larger difference of 0.08 dex for SN2002jz are likely caused by very different seeing conditions (1.2 arcsec versus 0.8 arcsec) between the two observations in 2016 and 2019.

The consistency of results over different observing runs for the same SNe gives us confidence in the results of the relative metallicities and subtype distributions.

5.3 Reliability of N2 and O3N2 results

The application of the strong emission lines method is restricted to gas phase emission caused by stellar ionization. We checked this precondition by means of the BPT-diagram (Baldwin, Phillips & Terlevich 1981) shown in Fig. 6. All targets with O3N2 results are well within the H II region; for targets with N2 results only, the BPT diagram is not applicable.

The mean and standard deviations for the N2 and O3N2 calibrations, presented in Table 3 exhibit small quantitative differences between the two calibration methods. First, the standard deviations of Type Ib differ from the other two SN subtypes by 0.07 dex for N2 and 0.1 dex for O3N2, and secondly the mean metallicities determined from the O3N2 calibration for the Types Ibc are both ~0.08 dex larger than the Type IIP mean metallicity, however no differences are identified using the N2 calibration. It is unclear why the two calibrations present different results. It could be caused by the larger number of N2 results (65 N2 results compared with 46 O3N2 results), by differences between the two calibration methods or an indication of real distinctions between the environments of different SN types that are only detectable with the O3N2 calibrator as a result of using more spectral information than the N2 calibration. Investigating the source of these differences is beyond the scope of this work and requires additional data.

The N2 and O3N2 calibrations (equations 3 to 6) are derived from empirical data and as such each calibration is only valid over a certain range. The validity ranges for the N2 and O3N2 indicators from Marino et al. (2013) and Pettini & Pagel (2004) are converted into terms of absolute metallicity and presented in Table 5. Comparison of the SN metallicity results in Table A2 with the corresponding validity range of M13-O3N2 and PP04-O3N2 calibrations show that no SN lies outside of the validity interval when taking into account the calibration uncertainties of $\pm$0.18 dex and $\pm$0.14 dex, respectively

[6] http://research.iac.es/proyecto/miles/pages/ssp-models.php

Downloaded from https://academic.oup.com/mnras/article/512/1/1541/6545806 by University of Central Lancashire user on 23 March 2022

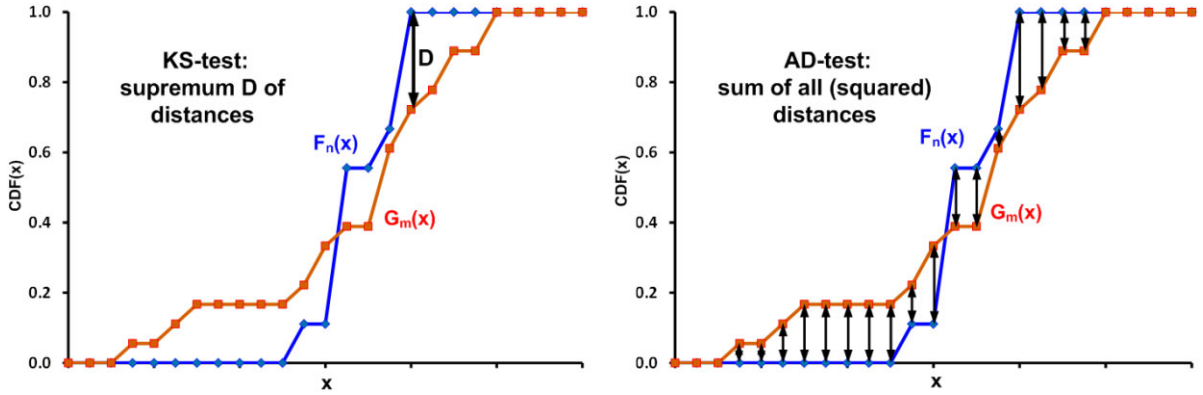

Figure 4. Approach of the two-sample KS-test (left-hand panel) and of the two-sample AD-test (right-hand panel) to test the null hypothesis that two samples are drawn from same parent population. The KS-test uses only the supremum of absolute values of the distances between two CDFs to test the null hypothesis. The AD-test uses the sum of all (squared) distances between two CDFs to judge the null hypothesis. Compared with KS-test, the AD-test is more sensitive to CDF differences in the tails.

Table 4. *P*-values of the two-sample KS-test and two-sample AD-test for the M13 results calculated by the functions 'ks_test' and 'ad_test' of the R-project package 'twosamples'. All *p*-values exceed the chosen significance level of 5 per cent and the null hypothesis that the two samples are drawn from same parent population cannot be rejected.

SN type	KS-test		AD-test	
	M13-N2 *p*-value	M13-O3N2 *p*-value	M13-N2 *p*-value	M13-O3N2 *p*-value
Ib-Ic	0.766	0.704	0.669	0.483
Ib-IIP	0.723	0.128	0.449	0.137
Ic-IIP	0.278	0.309	0.452	0.258
Ib-(Ic + IIP)	0.749	0.311	0.583	0.279

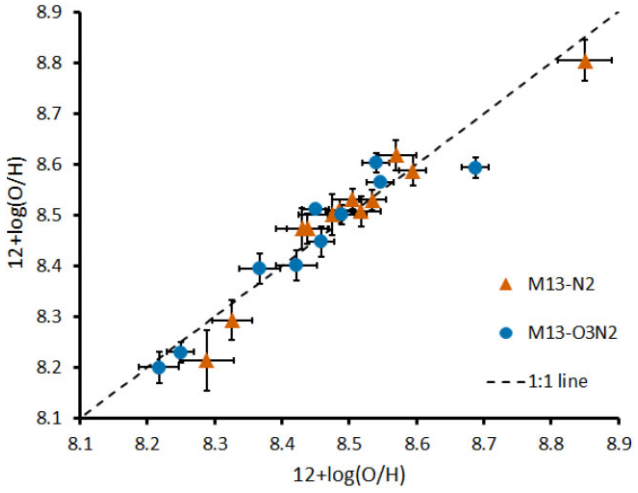

Figure 5. Scatter plot of INT targets observed multiple times. The figure shows metallicities of first observations versus second observations. For targets with three observations, the worst case difference is shown. The time interval between the two observations was at least eight months. The error bars indicate the uncertainties caused by photon noise and data reduction process only and do not include the calibration uncertainties, which dominate the overall uncertainty (see Table A2). The dashed line represents the hypothetical 1:1 line expected for identical values.

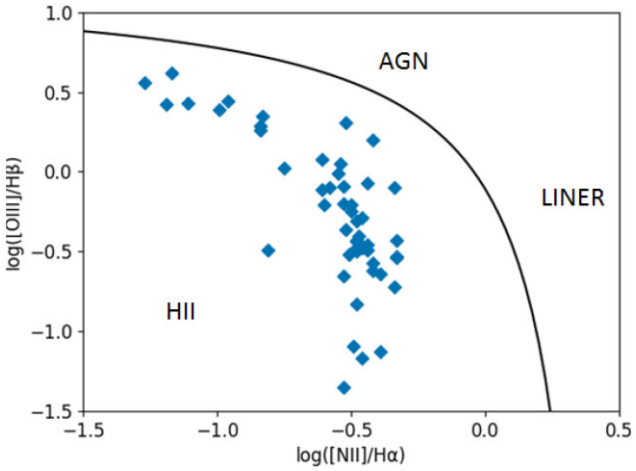

Figure 6. BPT-diagram of all targets with O3N2 calibration (blue diamonds). The black solid line is the decision line between the H II region and the AGN/LINER region as given by Kewley et al. (2001) (their equation 5). All targets are well within the H II region of the BPT-diagram.

Table 5. Validity limits of M13 and PP04 calibrations as given in Marino et al. (2013) and Pettini & Pagel (2004), respectively. N2 and O3N2 given by equations (1) and (2), respectively.

Calibration	Validity limits	12 + log(O/H) validity limits
M13-N2	$-1.6 < N2 < -0.2$	$8.00 < 12 + \log(O/H) < 8.65$
M13-O3N2	$-1.1 < O3N2 < 1.7$	$8.17 < 12 + \log(O/H) < 8.77$
PP04-N2	$-2.5 < N2 < -0.3$	$7.48 < 12 + \log(O/H) < 8.73$
PP04-O3N2	$-1.0 < O3N2 < 1.9$	$8.12 < 12 + \log(O/H) < 9.05$

For the M13-N2 calibration eight SN lie outside of the validity range, however all but two (SN2000ds and SN2012cw) are within the metallicity calibration uncertainty of ±0.16 dex. Nine SN metallicities determined using the PP04-O3N2 calibration lie outside its validity range and four exceed the upper validity limit even when taking into account the ±0.18 dex calibration uncertainties. These SN are SN2000ds and SN2012cw, consistent with M13-N2, and also SN1999em and SN2014bc. SN2014bc is very close (about 160 pc) to the active galactic nuclei (AGNs) of its host NGC 4258 and the spectrum may be contaminated by non-thermal radiation from the

Downloaded from https://academic.oup.com/mnras/article/512/1/1541/6545806 by University of Central Lancashire user on 23 March 2022

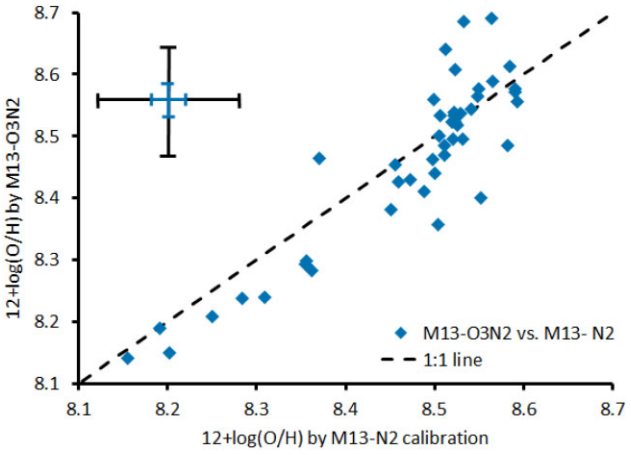

Figure 7. Comparison of metallicity for SN where results using both the M13-O3N2 and M13-N2 calibrations is available. The black cross at top left-hand side indicates the overall uncertainty of the metallicities dominated by the calibration uncertainties; the overlaid blue cross indicates the typical observational uncertainty. The dashed line represents the hypothetical 1:1 line expected for identical values. There is an apparent pileup of points for x-axis values > 8.5 dex, where the scatter significantly increases.

AGN. The hosts of SN1999em and SN2012cw have AGNs as well, but the SNe are likely to be too distant for non-thermal contamination of the spectrum and as noted before SN2000ds is a Ca-rich SN. Unfortunately it is not possible to plot any of these SNe on the diagnostic BPT diagram presented in Fig. 6 since no H β emission is detected. The effect of outliers on the statistical evaluation results of our N2 sample was checked by tentatively varying their metallicity. Any differences are negligible and thus we conclude that the validity ranges have no impact on our overall findings.

To test the consistency between the two calibrations (M13-O3N2 and M13-N2), we compare the metallicity of each SN calculated with each calibration; the results are presented in Fig. 7. It is clear that there is generally a good linear agreement between the calibrations (linear regression coefficient ∼76 per cent) but an increasing scatter with increasing metallicity is present. This scatter may be caused by the relatively small number of targets in the lower metallicity range and/or by the limitations of the N2 calibration at higher metallicities.

The differences between the N2 and the O3N2 results may have a physical background. As highlighted by e.g. Pettini & Pagel (2004) and Marino et al. (2013), the [N II] line saturates for metallicities greater than solar metallicity (12 + log(O/H) = 8.69; Asplund et al. 2009) while the [O III] line does not. Consequently, the N2 calibration should be unreliable for high metallicities as it relies just on [N II]. This larger uncertainty of the N2 calibration at high metallicities is consistent with the larger scatter at higher metallicities in Fig. 7. However, the spread, potentially indicating saturation effects, starts at about 8.5 dex, well below solar metallicity. The N2 calibration is known to produce scatter above solar metallicity but our work suggests that these effects could be present at lower metallicities of ∼8.5 dex, however given the large calibration errors it is difficult to draw any firm conclusions.

The number of outliers (6 per cent of total sample) is too small to explain the differences between the N2 and O3N2 results because the CDFs do not change significantly if the outliers are removed. The observed trends between SN subtypes in the CDFs are most likely not caused by an improper application of the strong emission lines methods.

5.4 Monte Carlo simulations

Results of the statistical significance tests presented in Table 4 are based on values of the metallicities for environment of the three SN subtypes. These values suffer from large uncertainties of ±0.16 dex and ±0.18 dex for M13-N2 and M13-O3N2, respectively and can ultimately lead to a large range of absolute values and thus a range of p-values. For example, Leloudas et al. (2011) performed Monte Carlo (MC) simulations perturbing the metallicity around the mean value and found $0.007 < p < 0.483$ at a 68 per cent confidence interval. Monte Carlo (MC) simulations have been applied to estimate the sensitivity of the p-values of the KS- and AD-test to the uncertainties of the metallicity results from the INT data.

The MC simulations were done by a simple algorithm as follows:

(i) take the vector a_1 of the nominal metallicity values of the first SN type and add a random vector (representing the possible effect of the uncertainty), where each vector component is randomly drawn from a Gaussian distribution with mean = 0.0 and standard deviation sigma = sd_1;
(ii) take the vector a_2 of the nominal metallicity values of the second SN type and add a random vector, where each vector component is randomly drawn from a Gaussian distribution with mean = 0.0 and sigma = sd_2;
(iii) apply the KS- and the AD-test to the vector a_1 and a_2;
(iv) repeat the three steps above for a large number N;
(v) create the histogram of the N calculated p-values of the KS- and of the AD-test.

The number N was chosen to be 20 000 as a reasonable choice between significance of the MC results and the required time. The standard deviations sd_1 and sd_2 were constant for each particular MC simulation, but they were changed between 0.0 and 0.18 dex (maximum uncertainty of the calibrations) for different MC runs to evaluate the distribution of the p-values at different uncertainties. As in Section 4, the 'R' package implementations of the KS- and the AD-test have been used to perform the tests in the MC runs.

The distributions of resulting p-values are presented in Fig. 8 and the range of possible p-values increases as the uncertainty increases. For observational uncertainties of ±0.04 dex p-values up to ∼0.5 for the KS-test are possible, which is similar to the range found by Leloudas et al. (2011). For the AD-test, p-values range between 0 and 0.6. However, for the uncertainties given by the strong emission line calibrations (±0.16 dex), all p-values between 0 and 1 are possible in both the KS- and AD-tests independent of the samples used. There is a clear qualitative difference between the distributions of p-values of the KS- and the AD-test: the KS-test distribution tends to a more multimodal distribution, the AD-test to a more continuous distribution of the p-values (see Fig. 8 for an example). We suggest that this could be due to use of a single supremum value in the KS-test in combination with the relatively small samples. However, this is beyond the scope of this paper. Taking into account the high sensitivity of the p-values to uncertainties, the application of the KS-test and/or AD-test is questioned if the samples under test suffer large uncertainties.

5.5 Constraints for type Ibc progenitors

The results for mean metallicities in Table 3 show no statistically significant difference between the three SN subtypes which is in a good agreement with previous studies by Anderson et al. (2010), Galbany et al. (2016c), Kuncarayakti et al. (2018), Leloudas et al. (2011), and Sanders et al. (2012). The results of Modjaz et al. (2011) and Kuncarayakti et al. (2013b), which found higher metallicities for Type Ic SNe

Downloaded from https://academic.oup.com/mnras/article/512/1/1541/6545806 by University of Central Lancashire user on 23 March 2022

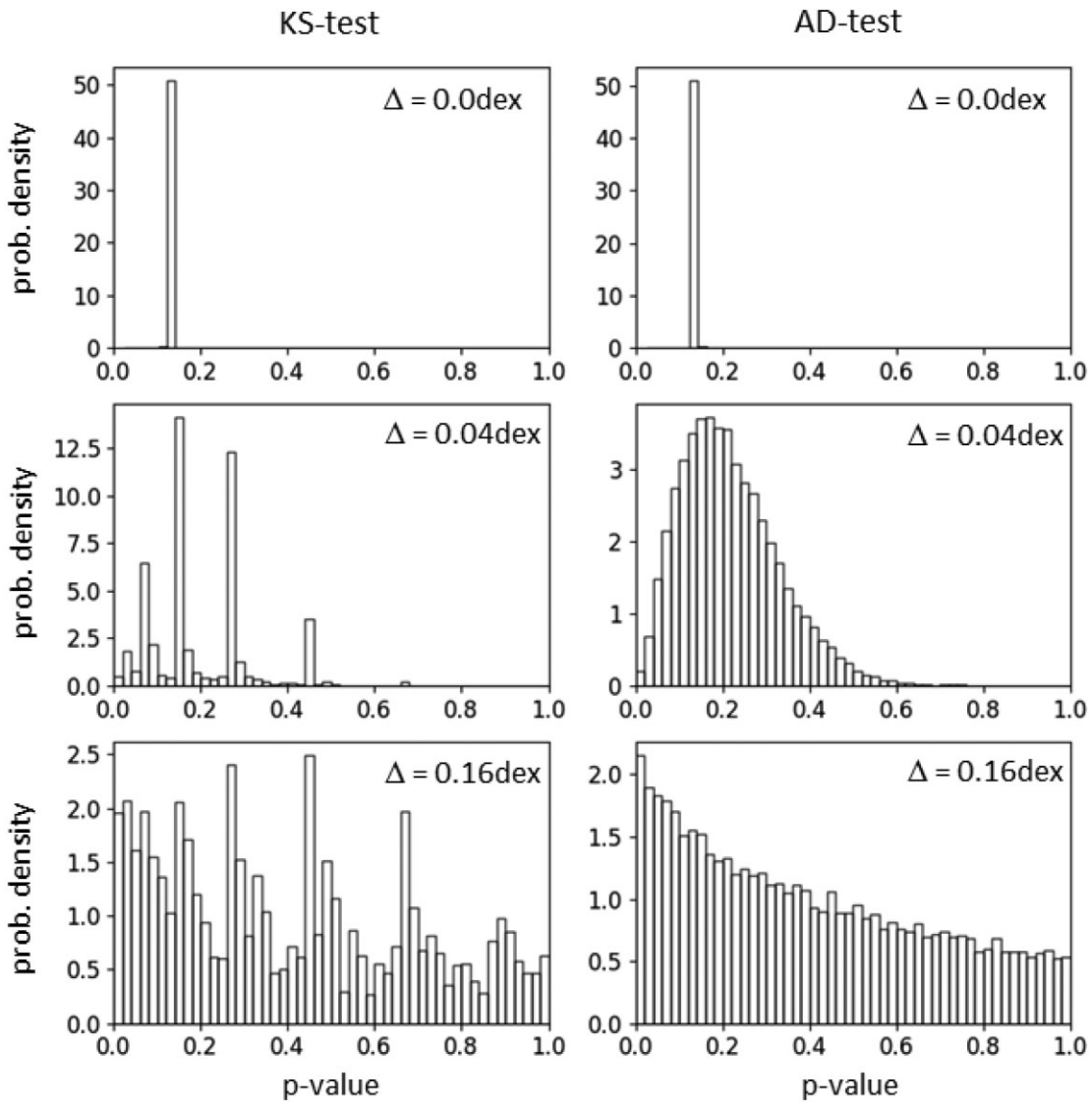

Figure 8. Representative example for the results of the MC simulations, based on perturbing our sample with differing levels of uncertainty. The figure shows six results of the MC simulations with three results of the KS-test (left-hand panel) and three results of the AD-test (right-hand panel). In all cases, the same samples of metallicity values have been used (Type Ib and Type IIP M13-O3N2 results). The number N of runs was 20 000 for all simulations. All plots show the probability density of p-values; the area of the histograms bins (bin width = 0.02) is normalized to one in all charts. The top row shows results for an uncertainty 0.0 dex with a single bin for the p-value as expected. In the middle row with an uncertainty of 0.04 dex (representative value for the observational and reduction process uncertainty) a significant broadening of the p-value distribution is visible already. Finally, in the bottom row with 0.16 dex uncertainty (the M13-N2 calibration uncertainty) all p-values as outcome of the tests are possible with high probability. The result shown is qualitatively the same for all sample combinations of Table 4.

compared with Type Ib SNe, could not be confirmed. As discussed in Section 4, there is only a slight metallicity difference of 0.08 dex between the Type Ibc and Type IIP SN for the M13-O3N2 calibration. This tendency is confirmed in the corresponding CDF (Fig. 3b), but the KS- and the AD-test in Section 4 revealed no statistical significance between the parent population of different SN subtypes in agreement with the KS-test results of Anderson et al. (2010), Galbany et al. (2016c), Kuncarayakti et al. (2018), Leloudas et al. (2011), Sanders et al. (2012), and the AD-test results of Galbany et al. (2018).

However, the MC simulation results of KS- and AD-test highlight the limitations of these two statistical tests as a result of the large uncertainties associated with the calibrations themselves; this is consistent with the findings of Leloudas et al. (2011) for the KS-test. Additionally, as for all statistical tests, if the test does not reject the null hypothesis, this does not conclusively mean that the alternative hypothesis is wrong.

For example, the distribution of Type Ib SNe metallicity environments is narrower than Type Ic and IIP (Fig. 3b). This finding is consistent with the CDFs of Kuncarayakti et al. (2018) and Galbany et al. (2018) giving some evidence of different physical qualities of Type Ib environments which implies different physical progenitors of Type Ib SN compared to Type Ic and IIP. To test this further, results for the Type Ib/Ic/IIP subsample[7] in Galbany et al. (2018) have been used. This subsample consists of 19 Type Ib, 20 Type Ic, and 31 Type

[7]the data of the total sample of Galbany et al. (2018) have been downloaded from https://iopscience.iop.org/article/10.3847/1538-4357/aaaf20

Downloaded from https://academic.oup.com/mnras/article/512/1/1541/6545806 by University of Central Lancashire user on 23 March 2022

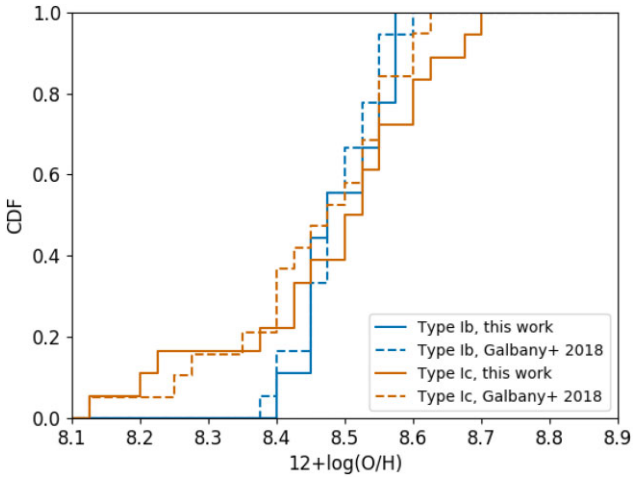

Figure 9. Comparison of Type Ib and Type Ic with M13-O3N2 calibration CDFs from this work (solid lines) and from the Type Ibc subsample of Galbany et al. (2018) (dashed lines). The CDFs for these almost completely distinct samples show very good agreement. Binning width for CDF calculation: 0.025 dex.

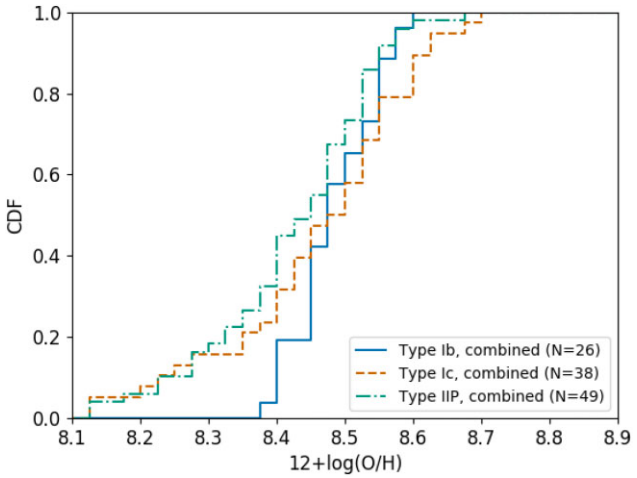

Figure 10. M13-O3N2 calibration CDFs of the combined sample of this work (including targets of Table A3) and the Type Ib/Ic/IIP subsample of Galbany et al. (2018). The four targets common in the two M13-O3N2 samples are replaced by the average value of both metallicities. Binning width for CDF calculation: 0.025 dex.

IIP, and it is almost completely distinct from our sample (only 5 IIP, 2 Ib, and 1 Ic SNe are common in both samples). Fig. 9 compares the Type Ib and Ic CDFs from this work with the corresponding CDFs of the Type Ib and Ic subsample of Galbany et al. (2018) for the M13-O3N2 calibration. The narrow Type Ib distribution and the broader Type Ic distribution starting at low metallicities seen in our work are confirmed by the Galbany et al. (2018) subsample.

Fig. 10 shows the M13-O3N2 calibration CDFs of the combined sample from this work (including the four targets of Table A3) plus the Galbany et al. (2018) subsample. The combined M13-O3N2 sample consists of 26 Type Ib, 38 Type Ic, and 49 Type IIP. It confirms our CDFs of Fig. 3 both qualitatively and quantitatively with a higher statistical significance because of the considerably larger sample size. The mean metallicities and the standard deviations of the combined sample are shown in Table 6. The smaller standard deviation of

Table 6. Number of targets N, mean values, and standard deviations σ of the metallicities split into the three SN types and for the total sample based on the M13-N2 and M13-O3N2 calibrations for the results of our study combined with results from Galbany et al. (2018).

SN type	N(N2)	M13-N2 [12 + log(O/H)] mean	σ	N(O3N2)	M13-O3N2 [12 + log(O/H)] mean	σ
Ib	31	8.52	0.06	26	8.50	0.06
Ic	40	8.49	0.13	38	8.47	0.14
IIP	60	8.49	0.13	49	8.44	0.12
all	131	8.50	0.12	113	8.46	0.12

Table 7. P-values of the two-sample KS-test and two-sample AD-test for the M13 results of our study combined with results from Galbany et al. (2018). The results of statistical tests on the combined sample indicate a statistically significant difference of the O3N2 results of Type Ib versus IIP and Type Ib versus Ic + IIP for a significance level of 5 per cent. All other cases indicate no significant difference.

	KS-test		AD-test	
SN types	M13-N2 p-value	M13-O3N2 p-value	M13-N2 p-value	M13-O3N2 p-value
Ib-Ic	0.245	0.311	0.138	0.086
Ib-IIP	0.120	0.027	0.077	0.020
Ic-IIP	0.788	0.189	0.853	0.165
Ib-(Ic + IIP)	0.088	0.056	0.082	0.037

the Type Ib results compared with Types Ic and IIP, as seen in Table 3, is confirmed in the combined sample. The KS- and AD-test of the combined sample (Table 7) indicate a statistically significant difference of the O3N2 results between Type Ib versus IIP and Type Ib versus Ic + IIP at a significance level of 5 per cent. All other test results indicate no significant differences below a 5 per cent level.

We note that these statistical tests are still subject to the large calibration uncertainties as discussed in Section 5.4. However, accepting the limitations of the KS- and AD-tests, is it possible to draw any conclusions regarding the progenitors of the different SN subtypes based on the CDF's and subsequent analysis? If the differences are indeed real, what do they represent?

Single massive stars have less physical parameters determining their mass-loss (essentially initial mass, metallicity, rotation, and magnetic field). Compared with single stars, compact binaries have additional orbital and evolutionary parameters of the companion influencing the mass-loss/overflow rate. For instance, a massive star with mass and metallicity to evolve as single star to a Type Ib SN, can evolve to Type Ic by additional mass-loss to its companion in a compact binary system – the number of evolutionary pathways of the massive star has been increased by the companion. Consequently, the larger number of physical parameters induces the expectation of a larger scatter (e.g. Xiao et al. 2019) and consequently of broader CDFs in metallicity for the binary scenario. Consequently, the narrower Type Ib CDFs seen in the Figs 3, 9, and 10 may be an indication that the single massive progenitor star fraction for Type Ib is larger than for Type Ic.

Type Ic SNe have a broad distribution starting at low metallicities, where it closely matches the Type IIP distribution for 12+log(O/H) < 8.3. Besides the broad distribution, the low metallicity limit for Type Ic is a second indication of a significant binary fraction of Type Ic SNe progenitors. Stripping H- and He-shells at low metallicities by

Downloaded from https://academic.oup.com/mnras/article/512/1/1541/6545806 by University of Central Lancashire user on 23 March 2022

stellar winds only is unlikely because the mass-loss strongly depends on metallicity (the higher metallicity the stronger mass-loss; e.g. Vink & Gräfener 2012). Thus, the binary scenario is favoured as the mass stripping mechanism at low metallicities. This conclusion is consistent with Smith et al. (2011a), who derived, based on standard IMFs and the observed fractions of core-collapse SNe, the necessity of binary progenitors. However, the single massive star formation channel for Type Ic SNe cannot be ruled out from our data and a mixture of both formation channels is likely.

While the agreement of the Type Ic and IIP CDFs at lower metallicity (e.g. this work; Galbany et al. 2018; Kuncarayakti et al. 2018) might seem contradictory given the single, massive nature of confirmed IIP progenitors (Smartt 2009; Van Dyk 2017), Type IIP progenitors have no need to lose their outer envelope allowing a broader range of masses and metallicities for single massive progenitors of Type IIP SN compared with Type Ib.

All constraints drawn above are not as distinctive for the N2 calibration results. However, it is reassuring that the CDFs created from data of the independent investigations by Galbany et al. (2018) are very similar (Fig. 9) to ours and that the CDFs of the combined sample (Fig. 10) still show the distinctive features. The combined samples produce a statistically significant rejection of our null-hypothesis for Ib-IIP SNe with $p = 0.027$ and $p = 0.020$ (see Table 7) for the KS- and AD-tests, respectively, as a result of increased sample size. More observations of SNe environments and metallicity calibrations with significantly lower uncertainties, supported by direct measurements of metallicities via massive stars (Davies et al. 2017) are still required to investigate all SN subtypes thoroughly and improve our understanding of core-collapse SNe progenitors.

6 SUMMARY AND CONCLUSIONS

This work calculates and compares the metallicities of environments of Type IIP, Type Ib, and Type Ic SNe within a luminosity distance of 30 Mpc by the strong emission line method. 76 targets were observed with INT/IDS and metallicity was measured for 65 of these using the N2 and O3N2 calibrations. The CDFs based on O3N2 calibration exhibit distinct features: narrow Type Ib distribution, Type Ic at low metallicities, and higher mean metallicities for Ibc SN compared to IIP. However, taking into account measurement errors, the statistical tests (KS-test and AD-test) are formally unable to reject the null hypothesis that the different SN types come from the same parent population.

The results of our analysis have been confirmed and strengthened by the CDFs created from the Type Ib/Ic/IIP sample of Galbany et al. (2018) as well as by the CDFs of the large combined sample of this work and the Galbany et al. (2018) subsample. For the combined sample, both statistical tests indicate a statistically significant difference between the Type Ib and Type IIP M13-O3N2 results at 5 per cent significance level. This suggests that Ib and IIP SN do indeed have different progenitor populations.

This statistical result combined with the apparent shapes of CDFs (see Fig. 10), might be explained by a significant fraction of single massive stars as Type Ib progenitors and suggests a significant fraction of compact binaries as progenitors of Type Ic SNe because they are present in low metallicity environments. Despite the large sample size of observed SNe environments these indications need further investigation with more observations of SNe environments in future work, to verify the significance of our results.

MC simulations have shown that the large calibration uncertainties have a significant effect on the range of p-values possible for both the KS- and AD-tests. These uncertainties must be reduced through improved calibrations and investigation of the saturation of the [N II] emission line.

ACKNOWLEDGEMENTS

The work presented is based on observations made with the Isaac Newton Telescope. The Isaac Newton Telescope is operated on the island of La Palma by the Isaac Newton Group of Telescopes in the Spanish Observatorio del Roque de los Muchachos of the Instituto de Astrofísica de Canarias. We would like to thank Isaac Newton Group of Telescopes staff and our co-observers A. Brocklebank, T. Davison, A. de Burgos, L. Holden, D. Nespral, S. Percival, T. Wilson, and T. Zegmott for their contributions to the observation data. JLP, AES, and SMH-M acknowledge financial support through the Science and Technology Facilities Council (STFC) Panel for the Application of Telescope Time (PATT) travel grant (IDs ST/S005307/1 and ST/M00211X/1). Supernova data have been obtained from the Open Supernova Catalogue currently maintained by James Guillochon and Jerod Parrent. Host galaxy data have been obtained from the NASA/IPAC Extragalactic Database (NED), which is operated by the Jet Propulsion Laboratory, California Institute of Technology, under contract with the National Aeronautics and Space Administration. The research has made use of tools created by hard work of the astronomical community, acknowledged here by tool name and URL: IRAF (https://iraf.net), STARLINK (http://starlink.eao.hawaii.edu/starlink), HYPERLEDA (http://leda.univ-lyon1.fr), 'R'-project (http://www.R-project.org), PPXF (https://pypi.org/project/ppxf), MILES stellar library (http://miles.iac.es/pages/stellar-libraries/miles-library.php)

DATA AVAILABILITY

The data underlying this article will be shared on reasonable request to the corresponding author.

REFERENCES

Aldering G., Humphreys R. M., Richmond M., 1994, AJ, 107, 662
Anderson J. P., James P. A., 2008, MNRAS, 390, 1527
Anderson J. P., James P. A., 2009, MNRAS, 399, 559
Anderson J. P., Covarrubias R. A., James P. A., Hamuy M., Habergham S. M., 2010, MNRAS, 407, 2660
Anderson J. P. et al., 2014, ApJ, 786, 67
Anderson J. P., James P. A., Habergham S. M., Galbany L., Kuncarayakti H., 2015, Publ. Astron. Soc. Aust., 32, e019
Arcavi I. et al., 2010, ApJ, 721, 777
Asplund M., Grevesse N., Sauval A. J., Scott P., 2009, ARA&A, 47, 481
Baldwin J. A., Phillips M. M., Terlevich R., 1981, PASP, 93, 5
Barth A. J., van Dyk S. D., Filippenko A. V., Leibundgut B., Richmond M. W., 1996, AJ, 111, 2047
Benetti S. et al., 2016, MNRAS, 456, 3296
Bersten M. C. et al., 2014, AJ, 148, 68
Boissier S., Prantzos N., 2009, A&A, 503, 137
Cao Y. et al., 2013, ApJ, 775, L7
Cappellari M., 2017, MNRAS, 466, 798
Cappellari M., Emsellem E., 2004, PASP, 116, 138
Chen K.-J., 2021, Internat. J. Mod. Phys. D, 30, 2130001
Crockett R. M. et al., 2007, MNRAS, 381, 835
Crockett R. M. et al., 2008, MNRAS, 391, L5
Crowther P. A., 2007, ARA&A, 45, 177
Crowther P. A., 2013, MNRAS, 428, 1927
Currie M. J., Berry D. S., Jenness T., Gibb A. G., Bell G. S., Draper P. W., 2014, in Manset N., Forshay P., eds, ASP Conf. Ser. Vol. 485, Astronomical Data Analysis Software and Systems XXIII. Astron. Soc. Pac., San Francisco, p. 391

Downloaded from https://academic.oup.com/mnras/article/512/1/1541/6545806 by University of Central Lancashire user on 23 March 2022

Davies B. et al., 2017, ApJ, 847, 112
Dessart L., Hillier D. J., Livne E., Yoon S.-C., Woosley S., Waldman R., Langer N., 2011, MNRAS, 414, 2985
Dowd C., 2020, preprint (arXiv:2007.01360)
Eldridge J. J., Maund J. R., 2016, MNRAS, 461, L117
Eldridge J. J., Izzard R. G., Tout C. A., 2008, MNRAS, 384, 1109
Eldridge J. J., Fraser M., Maund J. R., Smartt S. J., 2015, MNRAS, 446, 2689
Elias-Rosa N. et al., 2010, ApJ, 714, L254
Elias-Rosa N. et al., 2011, AJ, 742, 6
Elias-Rosa N. et al., 2013, MNRAS, 436, L109
Fang Q., Maeda K., 2018, ApJ, 864, 47
Filippenko A. V., 1997, ARA&A, 35, 309
Filippenko A. V., Chornock R., Swift B., Modjaz M., Simcoe R., Rauch M., 2003, Int. Astron. Union Circ., 8159, 2
Fitzpatrick E. L., 1985, ApJ, 299, 219
Folatelli G. et al., 2016, ApJ, 825, L22
Foley R. J., Berger E., Fox O., Levesque E. M., Challis P. J., Ivans I. I., Rhoads J. E., Soderberg A. M., 2011, AJ, 732, 32
Fremling C. et al., 2014, A&A, 565, A114
Fruchter A. S. et al., 2006, Nature, 441, 463
Gal-Yam A., 2019, ARA&A, 57, 305
Gal-Yam A., Leonard D. C., 2009, Nature, 458, 865
Gal-Yam A. et al., 2005, ApJ, 630, L29
Galbany L. et al., 2016a, AJ, 151, 33
Galbany L. et al., 2016b, MNRAS, 455, 4087
Galbany L. et al., 2016c, A&A, 591, A48
Galbany L. et al., 2018, ApJ, 855, 107
Graham J. F., 2019, preprint (arXiv:1905.13197)
Groh J. H., Georgy C., Ekstrom S., 2013, A&A, 558, L1
Guillochon J., Parrent J., Kelley L. Z., Margutti R., 2017, ApJ, 835, 64
Gutiérrez C. P. et al., 2017, ApJ, 850, 89
Hakobyan A. A. et al., 2014, MNRAS, 444, 2428
Hakobyan A. A. et al., 2016, MNRAS, 456, 2848
Helou G., Madore B. F., Schmitz M., Bicay M. D., Wu X., Bennett J., 1991, in Albrecht M. A., Bennett J., eds, Astrophysics and Space Science Library, Vol. 171, Databases & On-line Data in Astronomy. Springer, Dordrecht, p. 89
Henry R. B. C., Worthey G., 1999, PASP, 111, 919
Hirai R., 2017, MNRAS, 466, 3775
Hummer D. G., Storey P. J., 1987, MNRAS, 224, 801
James P. A., Anderson J. P., 2006, A&A, 453, 57
Johnson S. A., Kochanek C. S., Adams S. M., 2017, MNRAS, 472, 3115
Kelly P. L., Kirshner R. P., 2012, ApJ, 759, 107
Kewley L. J., Ellison S. L., 2008, ApJ, 681, 1183
Kewley L. J., Dopita M. A., Sutherland R. S., Heisler C. A., Trevena J., 2001, ApJ, 556, 121
Kewley L. J., Nicholls D. C., Sutherland R. S., 2019, ARA&A, 57, 511
Kilpatrick C. D. et al., 2018, MNRAS, 480, 2072
Kilpatrick C. D. et al., 2021, MNRAS, 504, 2073
Krühler T., Kuncarayakti H., Schady P., Anderson J. P., Galbany L., Gensior J., 2017, A&A, 602, A85
Kudritzki R.-P., Puls J., 2000, ARA&A, 38, 613
Kuncarayakti H. et al., 2013a, AJ, 146, 31
Kuncarayakti H. et al., 2013b, AJ, 146, 30
Kuncarayakti H. et al., 2015, A&A, 579, A95
Kuncarayakti H. et al., 2018, A&A, 613, A35
Leloudas G. et al., 2011, A&A, 530, A95
Lunnan R. et al., 2017, ApJ, 836, 60
Lyman J. D., James P. A., Perets H. B., Anderson J. P., Gal-Yam A., Mazzali P., Percival S. M., 2013, MNRAS, 434, 527
Makarov D., Prugniel P., Terekhova N., Courtois H., Vauglin I., 2014, A&A, 570, A13
Maoz D., Mannucci F., Nelemans G., 2014, ARA&A, 52, 107
Marino R. A. et al., 2013, A&A, 559, A114
Marsaglia G., Tsang W. W., Wang J., 2003, J. Stat. Softw., 8, 1
Massey F. J., 1976, J. Differ. Equ., 22, 416
Maund J. R., 2018, MNRAS, 476, 2629
Maund J. R., Smartt S. J., 2005, MNRAS, 360, 288
Maund J. R., Smartt S. J., Kudritzki R. P., Podsiadlowski P., Gilmore G. F., 2004, Nature, 427, 129
Maund J. R., Smartt S. J., Schweizer F., 2005, ApJ, 630, L33
Maund J. R. et al., 2011, ApJ, 739, L37
Mazzali P. A. et al., 2002, ApJ, 572, L61
Modjaz M. et al., 2008, AJ, 135, 1136
Modjaz M., Kewley L., Bloom J. S., Filippenko A. V., Perley D., Silverman J. M., 2011, ApJ, 731, L4
Osterbrock D. E., Ferland G. J., 2006, Astrophysics of Gaseous Nebulae and Active Galactic Nuclei, 2nd edn. University Science Books, Sausalito, CA
Pandey S. B. et al., 2021, MNRAS, 507, 1229
Pettini M., Pagel B. E. J., 2004, MNRAS, 348, L59
Pettitt A. N., 1976, Biometrika, 63, 161
Podsiadlowski P., Joss P. C., Hsu J. J. L., 1992, ApJ, 391, 246
Prantzos N., Boissier S., 2003, A&A, 406, 259
Press W. H., ed., 1988, Numerical Recipes in C: the Art of Scientific Computing. Cambridge Univ. Press, Cambridge; New York
Prieto J. L., Stanek K. Z., Beacom J. F., 2008, ApJ, 673, 999
Sanders N. E. et al., 2012, ApJ, 758, 132
Sanders N. E. et al., 2015, ApJ, 799, 208
Schady P., Eldridge J. J., Anderson J., Chen T.-W., Galbany L., Kuncarayakti H., Xiao L., 2019, MNRAS, 490, 4515
Schlafly E. F., Finkbeiner D. P., 2011, ApJ, 737, 103
Schlegel E. M., 1990, MNRAS, 244, 269
Shen K. J., Quataert E., Pakmor R., 2019, ApJ, 887, 180
Smartt S. J., 2009, ARA&A, 47, 63
Smartt S. J., 2015, Publ. Astron. Soc. Aust., 32, e016
Smartt S. J., Vreeswijk P. M., Ramirez-Ruiz E., Gilmore G. F., Meikle W. P. S., Ferguson A. M. N., Knapen J. H., 2002, ApJ, 572, L147
Smith N., 2014, ARA&A, 52, 487
Smith N., Li W., Filippenko A. V., Chornock R., 2011a, MNRAS, 412, 1522
Smith N. et al., 2011b, AJ, 732, 63
Taddia F. et al., 2013a, A&A, 555, A10
Taddia F. et al., 2013b, A&A, 558, A143
Taddia F. et al., 2015, A&A, 580, A131
Taddia F. et al., 2016, A&A, 587, L7
Taddia F. et al., 2019, A&A, 621, A71
Tartaglia L. et al., 2017, ApJ, 836, L12
Teffs J. J., Prentice S. J., Mazzali P. A., Ashall C., 2021, MNRAS, 502, 3829
Tody D., 1986, in Goad L., ed., Proc. SPIE Conf. Ser. Vol. 0627, Instrumentation in Astronomy VI. SPIE, Bellingham, p. 733
Turatto M., 2003, in Weiler K., ed., Lecture Notes in Physics, Vol 598, Supernovae and Gamma-Ray Bursters. Springer-Verlag, Berlin, p. 21
Valenti S. et al., 2011, MNRAS, 416, 3138
Valenti S. et al., 2016, MNRAS, 459, 3939
Van Dyk S. D., 2017, RSPTA, 375, 20160277
Van Dyk S. D., Schuyler D., 1992, AJ, 103, 1788
Van Dyk S. D., Garnavich P. M., Filippenko A. V., Höflich P., Kirshner R. P., Kurucz R. L., Challis P., 2002, PASP, 114, 1322
Van Dyk S. D. et al., 2011, ApJ, 741, L28
Van Dyk S. D. et al., 2014, AJ, 147, 37
Van Dyk S. D., de Mink S. E., Zapartas E., 2016, ApJ, 818, 75
Van Dyk S. D. et al., 2018, ApJ, 860, 90
Vazdekis A., Sánchez-Blázquez P., Falcón-Barroso J., Cenarro A. J., Beasley M. A., Cardiel N., Gorgas J., Peletier R. F., 2010, MNRAS, 404, 1639
Vink J. S., de Koter A., 2005, A&A, 442, 587
Vink J. S., Gräfener G., 2012, ApJ, 751, L34
Vink J. S., Sander A. A. C., 2021, MNRAS, 504, 2051
Woosley S. E., Bloom J. S., 2006, ARA&A, 44, 507
Xiang D. et al., 2019, ApJ, 871, 176
Xiao L., Galbany L., Eldridge J. J., Stanway E. R., 2019, MNRAS, 482, 384
Yoon S.-C., Woosley S. E., Langer N., 2010, ApJ, 725, 940

Downloaded from https://academic.oup.com/mnras/article/512/1/1541/6545806 by University of Central Lancashire user on 23 March 2022

APPENDIX A: LIST OF OBSERVED SUPERNOVAE

Table A1. List of observed targets. The columns are the target name, target SN type, host galaxy name and morphology, luminosity distance D_L, absolute magnitude M_V of the host galaxies, the position angle PA of the target with respect to galaxy centre, the distance d_c of the target from host centre, the number N of observations, and the total exposure time.

Target	Type	Host	Host type	D_L (Mpc)	M_V (mag)	PA (°)	d_C (arcsec)	N	Exp. time (s)
1995bb	Ib/c	PGC1409128	Irr?	25.8	–	87.6	9.38	1	4800
1998bv	IIP	HS1035 + 4758	?	23.4	−16.0	215.8	5.18	1	3600
1998dl	IIP	NGC 1084	SA(s)c	16.7	−21.8	54.1	28.82	1	3600
1999eh	Ib	NGC 2770	SA(s)c	26.0	−21.7	238.0	15.27	1	3600
1999em	IIP	NGC 1637	SAB(rs)c	7.7	−20.6	227.0	23.76	1	3600
1999ev	IIP	NGC 4274	SB(r)ab	21.0	−21.7	315.6	42.29	1	3600
1999gi	IIP	NGC 3184	SAB(rs)cd	11.0	−21.0	358.5	61.22	1	4000
2000ds	Ib	NGC 2768	E6	17.0	−21.7	196.5	33.17	2	7200
2000ew	Ic	NGC 3810	SA(rs)c	16.0	−21.4	187.5	20.27	1	3600
2001B	Ib	IC391	SA(s)c	25.0	−20.4	238.5	6.70	3	10800
2001ci	Ic	NGC 3079	SB(s)c	15.0	−22.1	351.8	27.88	2	7200
2001fv	IIP	NGC 3512	SAB(rs)c	25.0	−20.5	223.5	23.85	1	4200
2002hh	IIP	NGC 6946	SAB(rs)cd	4.7	−14.8	207.5	129.63	1	3600
2002ji	Ib	NGC 3655	SA(s)c	26.0	−21.7	236.1	25.11	1	3600
2002jz	Ic	UGC2984	SBdm	22.9	–	197.5	3.88	2	7200
2003gd	IIP	NGC 628	SA(s)c	3.4	−20.4	175.6	159.57	1	3600
2003ie	IIP	NGC 4051	SAB(rs)bc	13.0	−21.3	101.4	93.26	1	1200
2003J	IIP	NGC 4157	SAB(s)b	15.7	−22.0	242.5	71.89	1	5400
2003Z	IIP	NGC 2742	SA(s)c	20.0	−21.6	346.3	32.42	1	5400
2004A	IIP	NGC 6207	SA(s)c	20.0	−20.5	305.7	26.59	1	3600
2004ao	Ib	UGC10862	SB(rs)c	26.0	−19.1	165.3	26.36	2	7200
2004bm	Ic	NGC 3437	SAB(rs)c	21.0	−21.3	296.1	5.69	1	3600
2004C	Ic	NGC 3683	SB(s)c	35.0	−20.8	303.3	20.40	1	3600
2004dg	IIP	NGC 5806	SAB(s)b	22.0	−22.0	261.0	21.85	1	3600
2004dj	IIP	NGC 2403	SAB(s)cd	3.5	−19.4	94.0	159.14	1	3600
2004dk	Ib	NGC 6118	SA(s)cd	20.0	−21.8	6.6	42.99	1	3600
2004ez	IIP	NGC 3430	SAB(rs)c	26.0	−21.7	68.8	50.08	1	4600
2004fc	IIP	NGC 701	SB(rs)c	19.0	−20.9	19.4	2.23	1	3600
2004gk	Ic	IC3311	Sdm	17.0	−18.3	31.6	3.64	1	3600
2004gn	Ic	NGC 4527	SAB(s)bc	12.6	−20.7	68.9	59.43	2	7200
2004gq	Ib	NGC 1832	SB(r)bc	16.0	−21.7	45.0	30.83	1	3600
2004gt	Ic	NGC 4038	SB(s)m	16.0	−21.8	255.4	38.57	1	3600
2005ad	IIP	NGC 941	SAB(rs)c	20.0	−19.1	28.3	52.23	1	3600
2005ay	IIP	NGC 3938	SA(s)c	18.0	−20.7	194.2	58.38	1	3600
2005cs	IIP	NGC 5194	SA(s)bc	6.1	−20.9	179.3	67.30	1	3600
2005cz	Ib	NGC 4589	E2	20.0	−21.6	119.2	13.34	1	3800
2005kl	Ic	NGC 4369	SA(rs)a	21.0	−21.1	306.7	7.52	1	4800
2005V	Ib/c	NGC 2146	SB(s)ab	17.0	−22.1	24.8	4.19	1	3600
2006bp	IIP	NGC 3953	SB(r)bc	17.0	−22.3	33.9	112.49	1	4000
2007aa	IIP	NGC 4030	SA(s)bc	23.0	−22.3	41.9	91.88	1	3600
2007av	IIP	NGC 3279	Sd	29.0	−21.8	155.0	12.90	2	7800
2007C	Ib	NGC 4981	SAB(r)bc	21.0	−21.5	157.9	23.75	1	4200
2007gr	Ic	NGC 1058	SA(rs)c	10.0	−17.5	303.1	28.75	3	10800
2007od	IIP	UGC12846	Sm	24.0	–	132.7	51.90	1	3600
2008D	Ib	NGC 2770	SA(s)c	26.0	−21.7	325.3	67.27	2	7800
2008X	IIP	NGC 4141	SBcd	28.0	−18.9	60.1	9.22	1	3600
2009em	Ic	NGC 157	SAB(rs)bc	23.0	−21.7	251.8	33.90	1	3600
2009js	IIP	NGC 918	SAB(rs)c	16.0	−21.4	240.6	41.15	1	3600
2010br	Ib/c	NGC 4051	SAB(rs)bc	13.0	−21.3	124.4	17.50	1	4000
2010io	Ic	UGC4543	SAdm	29.0	−18.5	333.0	8.98	3	8400
2011ck	IIP	NGC 5425	Sd	30.7	−19.2	297.0	16.30	1	3600
2011dq	IIP	NGC 337	SB(s)d	24.4	−21.1	300.4	40.51	1	3600
2011jm	Ic	NGC 4809	Im	13.8	−17.3	93.8	1.50	1	3600
2012A	IIP	NGC 3239	IB(s)m	8.8	−19.7	133.9	49.57	1	4200
2012au	Ib	NGC 4790	SB(rs)c	20.0	−19.4	66.5	4.51	1	4200
2012bv	IIP	NGC 6796	Sbc	32.5	−21.0	187.4	30.25	1	4800
2012cw	Ic	NGC 3166	SAB(rs)a	19.9	−22.6	46.3	48.65	2	8400

Downloaded from https://academic.oup.com/mnras/article/512/1/1541/6545806 by University of Central Lancashire user on 23 March 2022

Table A1 – *continued*

Target	Type	Host	Host type	D_L (Mpc)	M_V (mag)	PA (°)	d_C (arcsec)	N	Exp. time (s)
2012ec	IIP	NGC 1084	SA(s)c	16.7	−21.8	358.9	15.00	1	3600
2012fh	Ic	NGC 3344	SAB(r)bc	8.6	−20.4	160.1	118.03	1	4200
2012P	Ib/c	NGC 5806	SAB(s)b	22.0	−22.0	256.5	19.73	1	4000
2013ab	IIP	NGC 5669	SAB(rs)d	23.6	−20.5	133.1	20.04	1	3600
2013bu	IIP	NGC 7331	SA(s)bc	12.1	−23.0	204.0	55.62	2	8400
2013dk	Ic	NGC 4038	SB(s)m	16.0	−21.8	194.6	15.81	1	4200
2013ej	IIP	NGC 628	SA(s)c	3.4	−20.4	134.1	127.87	1	4800
2013ff	Ic	NGC 2748	SAbc	21.9	−21.0	215.6	24.84	1	3600
2013ge	Ic	NGC 3287	SB(s)d	19.3	−18.4	18.7	50.56	2	6600
2014A	IIP	NGC 5054	SA(s)bc	27.0	−21.4	57.1	14.72	1	3600
2014bc	IIP	NGC 4258	SAB(s)bc	6.6	−21.9	141.7	3.44	1	4200
2014bi	IIP	NGC 4096	SAB(rs)c	8.3	−21.1	20.4	54.95	1	4200
2014C	Ib	NGC 7331	SA(s)bc	12.1	−23.0	140.6	31.19	1	3600
2014cx	IIP	NGC 337	SB(s)d	24.4	−21.1	303.6	40.51	1	3600
2015aq	IIP	UGC5015	SABdm	24.0	−18.5	267.5	43.05	1	4200
2015V	IIP	UGC11000	S?	20.3	−18.5	142.1	8.87	1	3600
2016bau	Ib	NGC 3631	SA(s)c	17.1	−19.5	293.5	37.95	1	3600
2017ein	Ic	NGC 3938	SA(s)c	18.0	−20.7	74.2	42.53	1	3600
2017iro	Ib	NGC 5480	SA(s)c	27.5	−21.3	125.0	17.74	1	3600

Table A2. Metallicities of the observed SNe environments. The columns are the target name, target SN type, the J2000.0 target coordinates, and the measured environment metallicities by N2 and O3N2 method based on the M13 calibration. The metallicities based on the older PP04 calibration are given as well for better comparability with previous studies. The uncertainties are dominated by the calibration uncertainties in all cases, which are ±0.16 dex for M13-N2, ±0.18 dex for M13-O3N2, ±0.18 dex for PP04-N2, and ±0.14 dex for PP04-O3N2 (all uncertainties are 1σ values as given in Marino et al. 2013 and Pettini & Pagel 2004, respectively, and correspond to the uncertainty on the final metallicity).

Target	Type	SN RA [h m s]	SN Dec [° ′ ″]	M13-N2 12 + log(O/H)	M13-O3N2 12 + log(O/H)	PP04-N2 12 + log(O/H)	PP04-O3N2 12 + log(O/H)
1998bv	IIP	10 38 25.40	+ 47 42 32.8	8.19	8.19	8.22	8.21
1998dl	IIP	02 46 01.47	−07 34 25.1	8.52	8.52	8.62	8.72
1999eh	Ib	09 09 32.67	+ 33 07 16.9	8.50	–	8.61	–
1999em⋆	IIP	04 41 27.04	−02 51 45.2	8.77	–	8.93	–
1999gi	IIP	10 18 16.66	+ 41 26 28.2	8.42	–	8.51	–
2000ds[1, ⋆]	Ib	09 11 36.24	+ 60 01 42.2	8.85	–	9.03	–
2000ew	Ic	11 40 58.52	+ 11 27 55.9	8.50	8.71	8.60	8.99
2001B	Ib	04 57 19.24	+ 78 11 16.5	8.51	8.49	8.61	8.65
2001ci	Ic	10 01 57.33	+ 55 41 14.6	8.59	8.57	8.71	8.79
2001fv	IIP	11 04 01.66	+ 28 01 55.7	8.71	–	8.86	
2002hh	IIP	20 34 44.29	+ 60 07 19.0	8.52	8.54	8.63	8.74
2002ji	Ib	11 22 53.15	+ 16 35 10.0	8.53	8.54	8.64	8.74
2002jz	Ic	04 13 12.52	+ 13 25 07.3	8.25	8.21	8.29	8.24
2003gd	IIP	01 36 42.65	+ 15 44 20.9	8.68	–	8.83	–
2003J	IIP	12 10 57.72	+ 50 28 31.8	8.67	–	8.81	–
2003Z	IIP	09 07 32.46	+ 60 29 17.5	8.55	8.40	8.66	8.53
2004A	IIP	16 43 01.90	+ 36 50 12.5	8.50	–	8.59	–
2004ao	Ib	17 28 09.35	+ 07 24 55.5	8.49	8.41	8.59	8.55
2004bm	Ic	10 52 35.33	+ 22 56 05.5	8.56	8.69	8.68	8.97
2004C	Ic	11 27 29.72	+ 56 52 48.2	8.52	8.52	8.63	8.72
2004dg	IIP	14 59 58.96	+ 01 53 25.6	8.53	8.68	8.64	8.96
2004dj	IIP	07 37 17.02	+ 65 35 57.8	8.50	8.36	8.61	8.47
2004dk	Ib	16 21 48.93	−02 16 17.3	8.37	8.46	8.44	8.63
2004fc	IIP	01 51 03.85	−09 42 06.9	8.55	8.56	8.66	8.78
2004gk	Ic	12 25 33.23	+ 12 15 40.1	8.50	8.44	8.60	8.59
2004gn	Ic	12 34 12.10	+ 02 39 34.4	8.51	8.64	8.62	8.89
2004gq	Ib	05 12 04.81	−15 40 54.2	8.55	8.58	8.66	8.80
2004gt	Ic	12 01 50.37	−18 52 12.7	8.53	8.52	8.63	8.71
2005ay	IIP	11 52 48.07	+ 44 06 18.4	8.56	8.59	8.68	8.81
2005cs	IIP	13 29 52.78	+ 47 10 35.7	8.44	–	8.52	–

Downloaded from https://academic.oup.com/mnras/article/512/1/1541/6545806 by University of Central Lancashire user on 23 March 2022

Table A2 – *continued*

Target	Type	SN RA [h m s]	SN Dec [° ′ ″]	M13-N2 12 + log(O/H)	M13-O3N2 12 + log(O/H)	PP04-N2 12 + log(O/H)	PP04-O3N2 12 + log(O/H)
2005kl	Ic	12 24 35.68	+ 39 23 03.5	8.51	8.53	8.61	8.73
2005V	Ib/c	06 18 38.28	+ 78 21 28.8	8.59	8.56	8.71	8.76
2006bp	IIP	11 53 55.74	+ 52 21 09.4	8.54	8.54	8.65	8.75
2007aa	IIP	12 00 27.69	−01 04 51.6	8.50	8.50	8.61	8.68
2007av	IIP	10 34 43.17	+ 11 11 38.3	8.59	–	8.72	–
2007C	Ib	13 08 49.30	−06 47 01.0	8.59	8.58	8.71	8.80
2007gr	Ic	02 43 27.98	+ 37 20 44.7	8.50	8.56	8.60	8.77
2008D	Ib	09 09 30.65	+ 33 08 20.3	8.46	8.45	8.55	8.61
2008X	IIP	12 09 48.33	+ 58 51 01.6	8.28	8.24	8.33	8.29
2009em	Ic	00 34 44.53	−08 23 57.6	8.52	8.53	8.63	8.73
2009js	IIP	02 25 48.28	+ 18 29 25.8	8.49	–	8.59	–
2010io	Ic	08 43 21.41	+ 45 44 18.0	8.31	8.24	8.36	8.29
2011ck	IIP	14 00 46.24	+ 48 26 45.4	8.46	8.43	8.55	8.57
2011dq	IIP	00 59 47.75	−07 34 20.5	8.36	8.30	8.42	8.38
2011jm	Ic	12 54 51.10	+ 02 39 14.9	8.15	8.14	8.17	8.14
2012A	IIP	10 25 07.39	+ 17 09 14.6	8.20	8.15	8.23	8.16
2012au	Ib	12 54 52.18	−10 14 50.2	8.50	8.46	8.60	8.62
2012bv	IIP	19 21 30.36	+ 61 08 12.0	8.58	8.48	8.70	8.66
2012cw⋆	Ic	10 13 47.95	+ 03 26 02.6	8.83	–	9.00	–
2012ec	IIP	02 45 59.88	−07 34 27.0	8.52	8.50	8.63	8.67
2012fh	Ic	10 43 34.05	+ 24 53 29.0	8.47	8.43	8.57	8.57
2012P	Ib/c	14 59 59.12	+ 01 53 24.4	8.50	–	8.60	–
2013ab	IIP	14 32 44.49	+ 09 53 12.3	8.57	–	8.69	–
2013bu	IIP	22 37 02.17	+ 34 24 05.2	8.53	8.49	8.64	8.67
2013dk	Ic	12 01 52.72	−18 52 18.3	8.58	8.61	8.70	8.85
2013ej	IIP	01 36 48.16	+ 15 45 31.0	8.66	–	8.80	–
2013ff	Ic	09 13 38.88	+ 76 28 10.8	8.51	8.47	8.61	8.64
2013ge	Ic	10 34 48.46	+ 21 39 41.9	8.45	8.38	8.54	8.50
2014A	IIP	13 16 59.36	−16 37 57.0	8.55	–	8.67	–
2014bc⋆	IIP	12 18 57.71	+ 47 18 11.3	8.78	–	8.95	–
2014bi	IIP	12 06 02.99	+ 47 29 33.5	8.60	–	8.72	–
2014C	Ib	22 37 05.60	+ 34 24 31.9	8.65	–	8.79	–
2014cx	IIP	00 59 47.83	−07 34 18.6	8.36	8.28	8.43	8.35
2015V	IIP	17 49 27.05	+ 36 08 36.0	8.36	8.29	8.42	8.37
2016bau	Ib	11 20 59.00	+ 53 10 25.6	8.54	–	8.65	–
2017ein	Ic	11 52 53.25	+ 44 07 26.2	8.52	8.61	8.63	8.84

Notes.[1] Classified as Ca-rich and excluded from statistical evaluations (see Section 4).
⋆ These SN metallicities lie outside of the validity range of the M13-N2 and/or PP04-N2 calibrations. See Section 5.3 for details.

Table A3. The metallicities of the four SNe environments observed by opportunity. See caption of Table A2 for the description of the columns and the uncertainties. These targets are not part of the statistical evaluation of our sample as they do not fulfill the selection criteria of the project, but they are included in the combined sample of our study and the Type Ib/Ic/IIP sample of Galbany et al. (2018).

Target	Type	SN RA [h m s]	SN Dec [° ′ ″]	M13-N2 12 + log(O/H)	M13-O3N2 12 + log(O/H)	PP04-N2 12 + log(O/H)	PP04-O3N2 12 + log(O/H)
1990aa	Ic	00 52 59.22	+ 29 01 48.3	8.40	8.37	8.47	8.49
1991ar	Ib	00 43 56.71	+ 01 51 13.5	8.49	8.42	8.59	8.56
1996D	Ic	04 34 00.30	−08 34 44.0	8.54	8.45	8.65	8.61
2009ga	IIP	23 28 26.78	+ 22 24 50.4	8.54	8.54	8.65	8.74

This paper has been typeset from a TEX/LATEX file prepared by the author.

Downloaded from https://academic.oup.com/mnras/article/512/1/1541/6545806 by University of Central Lancashire user on 23 March 2022